

Quantum Noise Spectroscopy of Critical Slowing Down in an Atomically Thin Magnet

Mark E. Ziffer^{¶, 1, 2, 3} Francisco Machado^{*}, ^{4, 5} Benedikt Ursprung^{*}, ² Artur Lozovoi^{*}, ^{6, 7} Aya Batoul Tazi^{*}, ¹ Zhiyang Yuan^{*}, ⁶ Michael E. Ziebel,³ Tom Delord,⁷ Nanyu Zeng,⁸ Evan Telford,³ Daniel G. Chica,³ Dane W. deQuilettes,^{9, 10}

Xiaoyang Zhu,³ James C. Hone,² Kenneth L. Shepard,⁸ Xavier Roy,³ Nathalie P. de Leon,⁶ Emily J. Davis,¹¹ Shubhayu Chatterjee,¹² Carlos A. Meriles,⁷ Jonathan S. Owen^{§, 3} P. James Schuck^{‡, 2} and Abhay N. Pasupathy^{†1, 13}

¹Department of Physics, Columbia University, New York, NY 10027 USA

²Department of Mechanical Engineering, Columbia University, New York, NY 10027 USA

³Department of Chemistry, Columbia University, New York, NY 10027 USA

⁴ITAMP, Harvard-Smithsonian Center for Astrophysics, Cambridge, MA 02138, USA

⁵Department of Physics, Harvard University, Cambridge, MA 02138, USA

⁶Department of Electrical and Computer Engineering, Princeton University, Princeton, NJ 08540, USA

⁷Department of Physics, CUNY, The City College of New York, New York, NY, 10031, USA

⁸Department of Electrical Engineering, Columbia University, New York, NY 10027 USA

⁹Division of Quantum Information and Integrated Nanosystems,

Massachusetts Institute of Technology, Lincoln Laboratory, Lexington, MA, 02421, USA

¹⁰Center for Quantum Engineering, Massachusetts Institute of Technology, Cambridge, MA, 02139, USA

¹¹Department of Physics, New York University, New York, NY 10003, USA

¹²Department of Physics, Carnegie Mellon University, Pittsburgh, PA 15213, USA

¹³Condensed Matter Physics and Materials Science Department, Brookhaven National Laboratory, Upton, NY, 11973 USA

Low frequency critical fluctuations in magnetic materials encode important information about the physics of magnetic ordering, especially in the associated critical exponents. While a number of techniques have been established to study magnetic critical fluctuations in bulk materials, few approaches maintain the required microscopic resolution, temporal range, and signal sensitivity to quantitatively analyze critical fluctuations in magnetic phases of 2D materials. Using nitrogen-vacancy (NV) centers in diamond as quantum probes, we implement T_2 (spin decoherence) noise magnetometry to quantitatively study critical dynamics in a tri-layer sample of the Van der Waals magnetic material CrSBr. We characterize critical fluctuations across the magnetic phase transition in CrSBr by analyzing the NV spin echo coherence decay on time scales that approach the characteristic fluctuation correlation time τ_c at criticality, allowing us to study the temperature dependence of critical slowing down. By modelling the spin echo decoherence using theoretical models for critical dynamics, we are able to extract the critical exponent ν for the correlation length. We find a value for ν which deviates from the Ising prediction and suggests the role of long-range dipolar interactions in modifying the critical behavior of magnetic fluctuation modes in CrSBr at the 2D limit. We further compare the divergence of correlation length in CrSBr to the predicted exponential divergence for 2D XY criticality, and find evidence suggesting the possibility of such behavior in a temperature window near T_C where static magnetic domains are absent. Our work provides a first demonstration of the capability of decoherence based NV noise magnetometry to quantitatively analyze critical scaling laws in 2D materials.

Near criticality, the macroscopic properties of an ordered phase often display features that are directly related to its microscopic interactions [1]. Notably, both static and dynamic correlations of the order parameter as a function of the physical parameter that tunes the transition, such as temperature or fields, exhibit universal scaling behavior near the critical point. Extracting the scaling functions and associated critical exponents can reveal a wealth of information about the microscopic interactions that lead to ordering, such as principal anisotropies, effective dimensionalities and interaction range. [1, 2]. In magnetic materials, key observables that exemplify such critical behavior are divergent correlation length (ξ) and time (τ_c) of order parameter fluctuations [2, 3]. The experimental characterization of fluctuation dynamics of magnetism has played key roles in understanding magnetic ordering in quantum materi-

als, and in establishing the universality of critical phenomena [3, 4]. At criticality magnetic order manifests in the form of fluctuating domains with sizes described by a spectrum of wavelengths $\lambda = q^{-1}$ (where q is wavenumber). To extract a critical exponent, one must employ experimental techniques that offer selectivity to fluctuations across a range of q to analyze variations in dynamics that are associated with the divergence of the characteristic correlation length ξ [3].

The recent discovery of stable magnetic phases in atomically thin Van der Waals (VdW) crystals has introduced new platforms to study the rich phenomenology of 2D magnets, and address open questions regarding magnetism in a bona-fide 2D setting. [5]. Unfortunately, atomically thin flakes of VdW magnets lack the sample volumes required to study magnetization dynamics using conventional techniques such as inelastic neutron scatter-

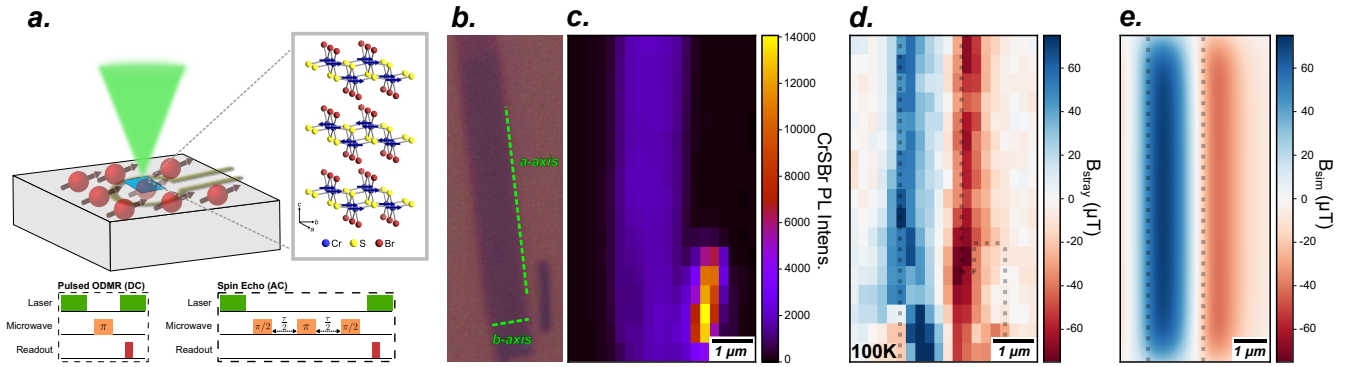


FIG. 1. (a). Schematic of the experimental sample configuration with a CrSBr flake (blue rectangle) transferred onto the surface of a ^{12}C diamond substrate with an NV ensemble (red spins) implanted at an average depth of $\sim 50\text{nm}$ (SI I). Inset shows the atomic and magnetic structure of a CrSBr tri-layer. Also shown are simplified pulse sequences for the DC and AC magnetometry techniques used in this work (see SI II C for full pulse sequences). (b). Brightfield optical image of the tri-layer CrSBr flake on a $\text{SiO}_2(285\text{ nm})/\text{Si}$ substrate. (c). Photoluminescence image (measured at 100 K) of the tri-layer CrSBr flake transferred onto the diamond substrate. The bright region in the lower right corresponds to another small multilayer flake, which can also be seen (b). (d). Stray field image of the tri-layer CrSBr flake at 100 K determined from the pulsed ODMR signal (SI II D). An outline of the flake based on co-registration with the PL image in (c) is shown by the grey dashed lines (SI II E). (e). Simulation of the stray field projection from a single uncompensated FM layer of CrSBr onto the depth distribution of our NV ensemble (SI III). The grey dashed outline represents the position of the simulated CrSBr flake.

ing, μSR , NMR, and EPR [3]. Quasi-elastic light scattering and magneto-optical techniques, recently applied to study critical fluctuations in 2D VdW magnets [6–8], are limited to probing very long wavelength fluctuations, which makes it challenging to resolve critical dynamics in the presence of static magnetic domains with dimensions below the optical diffraction limit.

Optically addressable solid-state spin-qubits are an emerging platform for sensing magnetism in mesoscopic materials, and are able to resolve fluctuations with wavelengths on the nm scale [9]. Seminal studies with the NV center in diamond have used T_1 relaxometry to probe fluctuations in condensed matter systems [10–13] including magnetic phases in 2D materials [14]. However, NV T_1 relaxometry achieves frequency tunability (in the GHz range) with the use of non-negligible external bias fields that may significantly alter the critical behavior in magnetic systems [10, 13]. Furthermore, it is necessary to study the noise spectral density in the MHz to sub-KHz range to access critical dynamics on time scales comparable to the fluctuation correlation time τ_c in many magnetic materials [3].

Recently it has been proposed that decoherence (T_2 noise) spectroscopy with the NV center could be used to quantitatively analyze critical dynamics and extract critical exponents in mesoscopic 2D magnets [15]. While T_2 and T_2^* based noise sensing are applied extensively with the NV center to characterize the spectral density of low frequency noise ($\sim \text{kHz-MHz}$) from fluctuating nuclear and electron spins in the bulk and surface spin-bath in diamond, and from target molecules on the diamond surface [16–23], only recently has NV T_2 noise sensing started to be employed to study fluctuations in magnetic phases of condensed matter systems [24].

In this work, we experimentally demonstrate the capability of NV ensembles to characterize critical dynamics and scaling laws of fluctuation correlations in a 2D VdW magnetic material CrSBr [25]. CrSBr is a VdW semiconductor with A-type layered antiferromagnetic (AFM) ordering below the bulk Néel temperature (T_N) at $\sim 132\text{ K}$ [26–29]. Below T_N the intralayer magnetic order is ferromagnetic (FM) with in-plane easy-axis ordering along the crystallographic b -axis, while interlayer AFM order forms along the c -axis from the stacking of individual layers with opposite intralayer FM magnetization (Figure 1a). In the thin film regime, even-number layers of CrSBr are purely AFM while odd-number layers posses a net magnetization from one uncompensated FM layer [30, 31].

We begin by using ensemble NV pulsed optically detected magnetic resonance (ODMR) (Figure 1a and SI I, II C for experimental details) to image the stray magnetic fields from a tri-layer CrSBr flake (Figure 1a,b). Measurements are performed with a small external bias field ($\sim 3.5\text{ mT}$) aligned along the NV spin quantization axis such that $|m_s = 0\rangle \rightarrow |m_s = -1\rangle$ resonances associated with one orientation of NV centers in the ensemble are selectively addressed with microwave pulses (SI II). Figure 1d shows a stray field image of tri-layer CrSBr at 100 K, along with an outline of the CrSBr flake determined from a simultaneously measured CrSBr photoluminescence image (Figure 1c and SI II E) [32]. As expected, we observe stray fields at the edges of the CrSBr flake consistent with in-plane magnetization along the b -axis from an uncompensated 2D FM layer [30, 31, 33]. The stray field image is in good agreement with simulations of the projection of the stray field from a single FM layer of CrSBr onto the NV spin-quantization axis measured in our ensemble

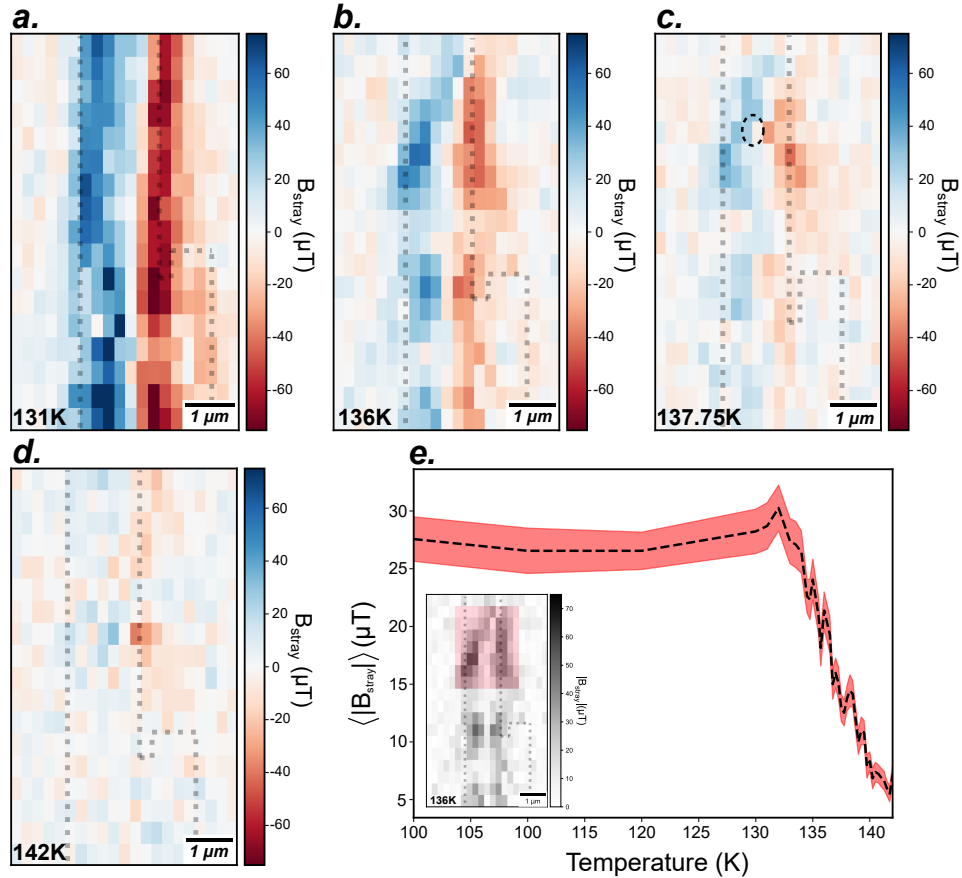


FIG. 2. (a-d). Stray field images of tri-layer CrSBr at temperatures across the magnetic phase transition. The gray dashed outlines represent the position of the CrSBr flake from co-registered CrSBr PL images (SI II E). The black circle in (c) represents the location within the flake where spin echo measurements are performed (see SI II E and IV for details). (e.) $\langle |B_{\text{stray}}| \rangle$ as a function of temperature across the CrSBr phase transition, calculated from pixels in the highlighted region of the $|B_{\text{stray}}|$ image in the inset. The width of the red shading on the $\langle |B_{\text{stray}}| \rangle$ curve represents the standard deviation of the mean from pixels used to calculate $\langle |B_{\text{stray}}| \rangle$.

(Figure 1e and SI III).

Next, we study the magnetic phase transition by imaging B_{stray} as a function of temperature with pulsed ODMR. Figure 2a shows the evolution of several representative stray field images across the phase transition. We observe the evolution of stray fields from an apparently uniformly magnetized domain below 132 K (Figure 1d and Figure 2a) to stray field patterns with μm -scale broken regions persisting over a temperature range of ~ 10 K (Figure 2b,c) before the stray field signal disappears at ~ 142 K (Figure 2d). The broken stray field patterns in the range of 132 – 142 K are consistent with μm scale magnetic domains that were observed to form across the phase transition in few-layer CrSBr with magnetic force microscopy and scanning single NV microscopy[30, 31]. The structure of these domains has been attributed to spatial variations in strain that affect the interlayer exchange coupling [30, 31]. To study the loss of magnetization across the phase transition, we define a region of pixels from one large-scale domain (Figure 2e, inset) and track the average absolute value of the

stray field($\langle |B_{\text{stray}}| \rangle$) as a function of temperature. Figure 2e shows the temperature dependence of $\langle |B_{\text{stray}}| \rangle$ from which we identify a characteristic phase transition temperature at ~ 140 K. We refer to this temperature as T_C (as opposed to T_N), as numerous studies on CrSBr have identified a characteristic temperature range where intralayer ferromagnetic correlations persist above T_N [25, 27, 28]. We point out that the small increase in $\langle |B_{\text{stray}}| \rangle$ at ~ 132 K may be related to the development of such ordering dominated purely by intralayer FM correlations [25].

To further study the phase transition, we correlate the temperature dependent static magnetic imaging with magnetic fluctuations measured by NV spin-echo decoherence. To this end, we prepare the NV spin in a coherent state $|\psi\rangle = \frac{1}{\sqrt{2}}(|0\rangle + |1\rangle)$, and allow it to evolve for a time period τ under the fluctuating magnetic field, such that $|\psi(\tau)\rangle = \frac{1}{\sqrt{2}}(|0\rangle + e^{-i\phi(\tau)}|1\rangle)$. We then evaluate the coherence decay $C(\tau) = e^{-\langle \phi^2(\tau) \rangle / 2}$, where $\langle \phi^2(\tau) \rangle$ is the variance of the stochastic phase over multiple exper-

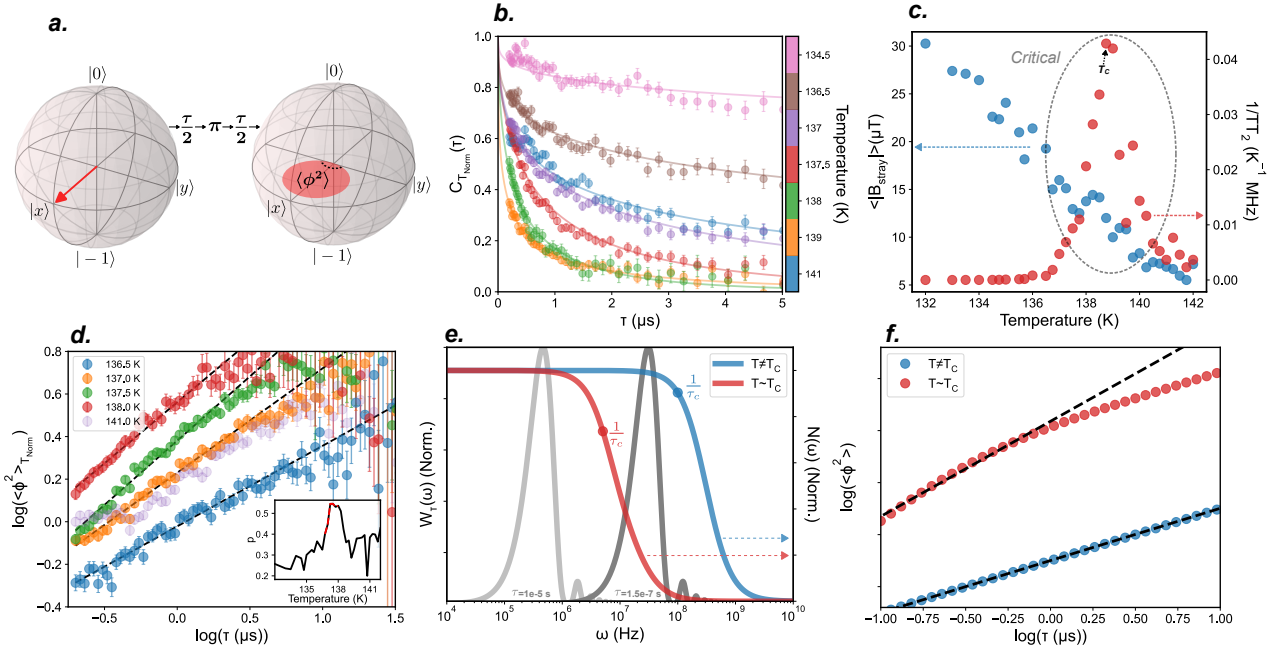


FIG. 3. (a). Bloch sphere representation of the the evolution of $\langle \phi^2(\tau) \rangle$ in the spin-echo experiment (note $|x\rangle = (|0\rangle + | -1\rangle)/\sqrt{2}$ and $|y\rangle = (|0\rangle + i| -1\rangle)/\sqrt{2}$). Note that $\pi/2$ pulses from the full $\pi/2_{(x)} \rightarrow \tau/2 \rightarrow \pi_{(y)} \rightarrow \tau/2 \rightarrow \pi/2_{(x,-x)}$ spin-echo pulse sequence (SI II C) are not shown. (b) Coherence decays $C_{T_{Norm}}(\tau)$ (with $T_{Ref} = 131\text{K}$) for several representative temperatures across the CrSBr phase transition. Also shown are the corresponding stretched exponential fits evaluated from $\tau = 0$ (solid lines). Based on our Rabi frequency (SI IV), the shortest τ that we select for measurements is 200 ns (c). Comparison of $\langle |B_{stray}| \rangle$ with $1/TT_2$ across the CrSBr phase transition, with T_C identified from the $1/TT_2$ peak at 138.75 K . The temperature range of critical fluctuations is $\sim 136.5 - 141\text{ K}$ (d). $\langle \phi^2(\tau) \rangle_{T_{Norm}}$ calculated from the data in (b). at selected temperatures in the range of critical fluctuations. Black dashed lines are linear fits to $\log(\langle \phi^2(\tau) \rangle_{T_{Norm}})$ vs. $\log(\tau)$. The change in slope of the linear fits to $\log(\langle \phi^2(\tau) \rangle_{T_{Norm}})$ vs. $\log(\tau)$ as a function of temperature corresponds to a change in power law scaling of $\langle \phi^2(\tau) \rangle_{T_{Norm}}$, which is reflected by a peak in the temperature dependence of the stretch power p of the coherence decay $C_{T_{Norm}}(\tau)$ (inset). The red trace in the inset highlights the temperature range of critical slowing down. (e.) Simulations of the noise spectral density at temperatures away (blue) and near (red) criticality, with characteristic frequencies $\omega_c = \tau_c^{-1}$ indicated. Also shown are spin echo filter functions $W_\tau(\omega)$ for two values of τ ($10\mu\text{s}$ and $0.15\mu\text{s}$) that approximately correspond to our experimental range. (f.) Simulation of $\langle \phi^2 \rangle$ as a function of spin echo free evolution time τ for the two different noise spectral density functions in (e), simulated over a range of τ spanning the limits of the filter functions in (e). We note that this range of τ does not sample the high-frequency region of the noise spectrum at criticality that would correspond to a regime of asymptotic behavior in the early-time log-log scaling of $\langle \phi^2(\tau) \rangle$ [23].

imental runs (Figure 3a) [15, 23]. The stochastic phase variance $\langle \phi^2(\tau) \rangle$ can be related to the noise spectral density from magnetic fluctuations $N(\omega)$ sensed by the NVs [15]:

$$\langle \phi^2(\tau) \rangle = \int_{-\infty}^{\infty} \frac{d\omega}{2\pi} W_\tau(\omega) N(\omega) \quad (1)$$

Here, $W_\tau(\omega)$ is a spectral filter function that depends on the free evolution period τ and is determined by the control pulse sequence (Figure 1a), which for spin echo is: $W_\tau(\omega) \propto \frac{\sin^4(\omega\tau/4)}{\omega^2}$ [15]. For a fixed pulse sequence and NV depth distribution, changes in the decay of the coherence can thus be related directly to changes in the spectral density of the magnetic noise.

We perform spin echo measurements at the center of the flake where $\langle |B_{stray}| \rangle$ is evaluated (indicated approximately by the black circle in Figure 2c, see SI II E for details). To quantify decoherence due to fluctuations from

CrSBr we define a temperature normalized coherence:

$$C_{T_{Norm}}(\tau) = \frac{C_T(\tau)}{C_{T_{Ref}}(\tau)} = e^{-\langle \phi^2(\tau) \rangle_{T_{Norm}}/2} \quad (2)$$

$$\langle \phi^2(\tau) \rangle_{T_{Norm}} = \langle \phi^2(\tau) \rangle_T - \langle \phi^2(\tau) \rangle_{T_{Ref}} \quad (3)$$

where the spin echo decays $C_T(\tau)$ and $C_{T_{Ref}}(\tau)$ are measured at the same location on the CrSBr flake at temperature T and a reference temperature T_{Ref} , respectively. Assuming that noise from the diamond spin bath adds a temperature independent background to $\langle \phi^2(\tau) \rangle_T$ and $\langle \phi^2(\tau) \rangle_{T_{Ref}}$ in the range of temperatures across the CrSBr phase transition, $\langle \phi^2(\tau) \rangle_{T_{Norm}}$ then quantifies the decoherence contributed solely from relative temperature dependent differences in the noise spectral density from fluctuations in CrSBr. [34]

Figure 3b shows $C_{T_{Norm}}(\tau)$ for a range of temperatures across the CrSBr phase transition normalized with

$T_{Ref} = 131$ K. A dramatic increase in the rate of coherence loss can be observed as T approaches ~ 139 K from temperatures both above and below T_C . We note that the temperature normalization fixes $C_{T_{Norm}}(\tau)$ at $\tau = 0$ to $C_{T_{Norm}}(0) = 1$ for temperatures within the range of $130 - 142$ K (taking into account both our Rabi frequency and inhomogeneous broadening of the NV ensemble, see SI IV). As such, we fit the data in this temperature range to a stretched exponential function $e^{-(\frac{\tau}{T_2})^p}$ (Figure 3b), with $\frac{1}{T_2}$ defined here as a decoherence rate due to the changes in magnetic noise from fluctuations in CrSBr as temperature is varied relative to T_{Ref} [35]. Using the fit values for $\frac{1}{T_2}$ we further determine a temperature weighted decoherence rate $\frac{1}{TT_2}$ which increases monotonically with the uniform magnetic susceptibility (χ_u) of CrSBr [15]. Figure 3c shows $\langle |B_{stray}| \rangle$ plotted against $\frac{1}{TT_2}$ for temperatures across the phase transition, from which we can precisely determine $T_C = 138.75$ K based on the peak of $\frac{1}{TT_2}$ that indicates the divergence in χ_u at a continuous transition. The trend of $\frac{1}{TT_2}$ shows a temperature range of critical fluctuations that spans from $\sim 136.5 - 141$ K (Figure 3d).

We also extract the stretch power p from the fits to $C_{T_{Norm}}(\tau)$. Interestingly, the extracted p is not monotonic, and exhibits a peak within the temperature range of critical fluctuations highlighting a concurrent change to the functional form of the decoherence signal (Figure 3d, inset). This is made apparent by plotting $\langle \phi^2(\tau) \rangle_{T_{Norm}}$ vs. τ on a log-log scale for temperatures in the range of critical fluctuations. In Figure 3d, $\langle \phi^2(\tau) \rangle_{T_{Norm}}$ shows a temperature dependent behavior near T_C that can be explained based on the evolution of the noise spectral density due to critical slowing down of the fluctuation correlation time τ_c [2, 15]. At temperatures sufficiently far away from criticality, scanning the spin echo filter function $W_\tau(\omega)$ over the experimental range of free evolution times τ samples a nearly flat region of the noise spectrum (blue trace, Figure 3e). Here, the resulting power law scaling of $\langle \phi^2(\tau) \rangle$ over the range of $\tau \sim 0.1 - 10 \mu s$ (blue trace, Figure 3f) is essentially temperature independent, as the characteristic frequency of the noise spectral density $\omega_c = \tau_c^{-1}$ is in the range of \gtrsim GHz. However, as critical slowing down of τ_c causes ω_c to enter the \sim MHz range near T_C (red trace, Figure 3e), the filter function $W_\tau(\omega)$ scans across a steep rise in the noise spectral density at low frequency and the power law scaling of $\langle \phi^2(\tau) \rangle$ (red trace, Figure 3f) becomes sensitive to the temperature dependence of τ_c . If we define $\langle \phi^2(\tau) \rangle = 2(\tau/T_2)^p$ based on a stretched exponential model, then a temperature dependent change in the power law scaling of $\langle \phi^2(\tau) \rangle$ corresponds to an effective change in p [15, 23].

Having identified a temperature window from the data indicating critical slowing down, we proceed to analyze the decoherence dynamics to determine a critical exponent. The noise spectral density $N(\omega)$ experienced by a single spin-qubit at a distance d below the 2D flake

is determined by the dynamical structure factor $S(q, \omega)$ that describes spatio-temporal fluctuations of the magnetic order parameter, and a momentum filter function $W_d(q) \propto q^3 e^{-2qd}$ that determines the sensitivity of the spin-qubit to fluctuations with momentum q [15]:

$$N(\omega) = \int_0^\infty W_d(q) S(q, \omega) \frac{dq}{2\pi} \quad (4)$$

We use a mean-field structure factor $S(q, \omega)$ for critical behavior of non-conserved order parameters, consistent with the anisotropies in the CrSBr Hamiltonian [2, 15, 36, 37]:

$$S(q, \omega) = \frac{2k_B T \Gamma_0}{\Gamma_0^2 J^2 (\xi^{-2} + q^2)^2 + \omega^2} \quad (5)$$

Here, J is the exchange energy, Γ_0 is a “kinetic coefficient” which is related to a characteristic low temperature fluctuation frequency ω_0 (see SI V A), and ξ is the correlation length [15]. Critical fluctuations are determined by the divergence of ξ , which exhibits a power-law scaling near T_C :

$$\xi = \xi_0 \left| \frac{T - T_C}{T_C} \right|^{-\nu} \quad (6)$$

where ν is the critical exponent and ξ_0 is a low temperature correlation length estimated from the CrSBr lattice constant (SI V A) [15]. Using Eqs (1–6) and a probability distribution function for NV depths in our ensemble (SI V A) we simulate $\langle \phi^2(\tau) \rangle_{T_{Norm}}^{ens}$ with $T_{Ref} = 136.75$ K over the temperature window of critical slowing down (Figure 4a, also see Figure 3d inset, red dashed trace) [38].

To determine the parameters ν , ω_0 , and J , the simulation is globally fit to the temperature dependent data in Figure 4a with T_C fixed at 138.75 K as determined from the $\frac{1}{TT_2}$ peak (Figure 3c). The resulting best fit value for $\omega_0 = 15.71$ GHz is in good agreement with the scale of magnon frequencies measured in CrSBr at low temperatures ($\sim 20 - 30$ GHz) [39, 40] and the value for $J = 7.5$ meV agrees with theoretical and experimental expectations for exchange constants in CrSBr. [25, 29] Turning our attention to the critical exponent, the best fit model gives a value $\nu = 0.73$. CrSBr is characterized by in-plane ferromagnetic order with magnetocrystalline anisotropy that favors easy-axis ordering along the b axis [27, 36, 41]; from this perspective, the critical behavior would be expected to fall under a 2D Ising transition where $\nu_{\text{Ising}} = 1$. However, we find that fitting with ν_{Ising} poorly reproduces the trends in the data (grey traces, Figure 4a), and the data can only be modelled using values of ν in the range of $\sim 0.6 - 0.8$ (see SI Section V B).

One explanation for the deviation of ν from the Ising value is the presence of long-range dipolar interactions, which are known to be important for capturing the magnetization dynamics in bulk CrSBr at low temperatures and for small- q [39]. Indeed, long-range dipolar interactions are also known to modify the critical dynamics

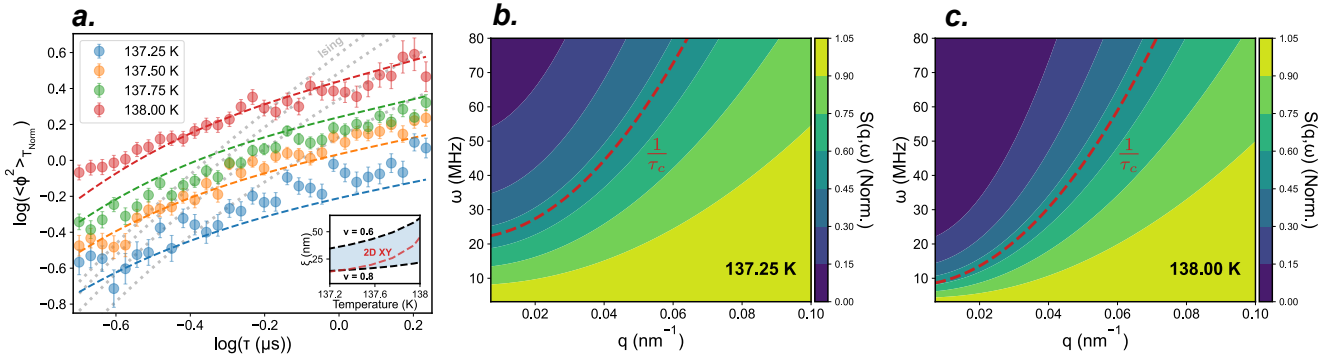


FIG. 4. (a). Data and mean-field simulation of $\langle \phi^2(\tau) \rangle_{T_{Norm}}^{ens}$ for temperatures in the window of critical slowing down, with $T_{Ref} = 136.75$ K used for temperature normalization of the coherence decay (Eq (2)) and SI V A). The best fit parameters from the mean-field simulation are $\nu = 0.73$, $\omega_0 = 15.71$ GHz, $J = 7.5$ meV (with T_C fixed at 138.75 K). Also shown is a simulation with ν fixed to the value of $\nu_{Ising} = 1$ (grey dashed curves, see SI V B). (Inset) Range of temperature dependent behavior of the correlation length ξ for $\nu = 0.6 - 0.8$ (indicated by the shaded blue region) compared with the behavior of ξ_{BKT} . A value of $b = 0.28$ is used to evaluate ξ_{BKT} with the formula $\xi_{BKT} = \xi_0 e^{b/\sqrt{(T-T_C)/T_C}}$. (b). and (c). Contour plots of the structure functions $S(q, \omega)$ evaluated for two temperatures at criticality (137.25 K and 138 K) using the best fit parameters from the simulation in (a.). The red dashed contour corresponds to the characteristic frequency $\omega_c(q) = \tau_c(q)^{-1}$, where $\tau_c(q)$ is the fluctuation correlation time (see SI Section V A). The shift of the $\tau_c(q)^{-1}$ contour to lower frequencies between (b.) and (c.) illustrates critical slowing down of the fluctuation correlation time as temperature approaches T_C .

away from the predictions from exchange-only models [3], with isotropic long-range interactions leading to a reduced value of ν [42, 43]. From this perspective, our results suggest that the effects of long-range dipolar interactions that influence magnetization dynamics in bulk CrSBr also extent to the 2D, few layer limit. Furthermore, it is important to note that both the easy-axis magnetocrystalline anisotropy and the dipolar interaction are quite small compared to both the XY exchange interaction in CrSBr and deviation from the critical temperature $\Delta T = T - T_C$ [36, 39]. In fact, evidence suggesting that the transition may be characterized by 2D XY criticality has been previously reported [26, 29]. To this end, we can compare our simulation results with expectations for XY-type critical behavior by evaluating the temperature dependence of the correlation length ξ . For the topological BKT transition associated with a 2D XY magnet, $\xi_{BKT} = \xi_0 e^{b/\sqrt{(T-T_C)/T_C}}$ diverges exponentially as $T \rightarrow T_C$ rather than following a power law [44][45, 46]. In the temperature window near T_C corresponding to our simulations, we find that ξ_{BKT} indeed falls in the range of behavior for the power law divergence of ξ (Eq (6)) with $\nu \sim 0.6 - 0.8$ (Figure 4a, inset). However, very close to T_C , the exponential divergence of ξ_{BKT} is likely to be affected by the presence of static domains on the $\lesssim 100$ nm length scale, which we believe form in our sample near criticality (SI IV) [31]. To fully characterize the universality class of the magnetic transition further studies would be needed to correlate fluctuation dynamics with the static domain structure on the nano-scale.

Finally, we explicitly determine the slowing down of the fluctuation correlation time by evaluating the structure factor at temperatures near criticality using the best fit parameters for ν , ω_0 , and J with $T_C =$

138.75 K. Figures 4b,c show the structure factor evaluated from Eqs (5) and (6) at 137.25 K and 138 K, along with a contour of the characteristic frequency $\omega_c(q)$, which corresponds to the inverse of the fluctuation correlation time $\tau_c(q)^{-1}$ (see SI Section V A). A comparison between the $\tau_c(q)^{-1}$ contours at 137.25 K and 138 K clearly demonstrates critical slowing down of the fluctuation correlation time in the range of small- q probed by our NV ensemble. In particular, the correlation time at 138 K (Figure 4c) starts to fall directly into the window of the free evolution times τ in our spin echo experiments, highlighting that the trends in the decoherence dynamics that we observe at criticality (Figures 3d, 4a) are indeed consistent with a physical model for the critical slowing down of fluctuations.

In conclusion, our work constitutes to a first foray into the quantitative analysis of critical phenomena in 2D materials using NV T_2 noise spectroscopy. As such, it highlights some crucial challenges and opportunities as this technique becomes more widely adopted. First, the form of $\langle \phi^2(\tau) \rangle^{ens}$ is highly sensitive to the NV depth distribution (SI V C), highlighting the need for NV ensemble with well characterized depth distributions (such as delta doped samples[23]). Moreover, techniques such as noise co-variance magnetometry may be advantageous as they rely on directly measuring fluctuation correlations between two spatially precise single NVs, avoiding the need to analyze fluctuation spatial correlations based solely on NV depths and associated q -space filter functions [47]. Second, we note that pulse sequences with filter functions that give higher spectral resolution (e.g. XY-8, CPMG) are desirable to better resolve the noise spectral density. In particular, structure factors are known to deviate significantly from mean-field models at tem-

peratures very close to T_C [1, 3], which could explain the trend in our data between $138.25\text{ K} - 138.75\text{ K}$ where the stretch exponent p and the decoherence rate $\frac{1}{T\tau_2}$ become anti-correlated approaching T_C (Figure 3d). Here, pulse sequence filter functions with high spectral resolution will be instrumental to characterize the more complex structure of $N(\omega)$.

Acknowledgments We thank Shaowen Chen, Nikola Maksimovic, Ruolan Xue, Laurens Vanderstraeten, Nick Bronn, Jennifer Schloss, Lin Pham, Mikael Backlund and Kristina Liu for fruitful discussions. We thank Daybis Tencio for obtaining the C-TRIM software and assisting in aspects of the sample preparation. M.E.Z was supported by Programmable Quantum Materials, an Energy Frontier Research Center funded by the U.S. Department of Energy (DOE), Office of Science, Basic Energy Sciences (BES) under award no. DE-SC0019443, along with seed funding support from Columbia University's Research Initiatives in Science and Engineering competition. J.S.O. was supported by the National Science Foundation (NSF) under CHE-2004008. A.N.P was supported by the Air Force Office of Scientific Research under grant FA9550-21-1-0378. A.B.T. was supported by the NSF under grant DMR-2004691. Work at Princeton was supported by the NSF (QuSEC-TAQS OSI 2326767 and Princeton University's Materials Research Science and Engineering Center DMR-2011750) and the Gordon and Betty Moore Foundation (grant DOI 10.37807/gbmf12237). T.D. acknowledges support by the DOE Office of Science, National Quantum Information Science Research Centers, Co-design Center for Quantum Advantage (C2QA) under contract number DE-SC0012704. A.L. and C.A.M. acknowledge support from the National Science Foundation, grant 1914945. C.A.M. also acknowledges support from the National Science Foundation, grant 2203904. F.M. acknowledges support from the NSF through a grant for ITAMP at Harvard University. S.C. acknowledges support from a PQI Community Collaboration Award.

Author contributions M.E.Z. conceived of the project with A.N.P., P.J.S., and J.S.O. M.E.Z. performed the experiments and analyzed the data with F.M., E.J.D., and S.C. M.E.Z. built the experimental apparatus with assistance from B.U. and designed the experiments with A.L., T.D., and C.A.M. Z.Y. and N.P.dL. processed the diamond used for ensemble NV magnetometry and A.B.T. fabricated the CrSBr flake on the diamond. D.G.C., E.J.T., Mi.E.Z., and X.R. synthesized and provided CrSBr crystals. N.Z. and K.L.S. assisted with testing the microwave PCB. D.W.D. grew and provided NV ensemble samples for initial experiments to verify the setup. X-Y.Z. and J.C.H. provided equipment and resources for experiments. A.N.P., P.J.S., and J.S.O. supervised the work. M.E.Z. wrote the manuscript. The manuscript reflects the contributions and ideas of all authors.

Competing interests The authors declare no competing interests.

Additional information

*F.M., B.U., A.L., A.B.T., and Z.Y. contributed equally to this work

Correspondence and requests for materials

[†]apn2108@columbia.edu

[‡]p.j.schuck@columbia.edu

[§]jso2115@columbia.edu

[¶]mz2733@columbia.edu

[1] J. Cardy, *Scaling and Renormalization in Statistical Physics* (Cambridge University Press, Cambridge, 1996).

[2] P. C. Hohenberg and B. I. Halperin, *Reviews of Modern Physics* **49**, 435 (1977).

[3] E. Frey and F. Schwabl, *Advances in Physics* **43**, 577 (1994).

[4] S. Sachdev, *Physics World* **12**, 33 (1999).

[5] Y. Ahn, X. Guo, S. Son, Z. Sun, and L. Zhao, *Progress in Quantum Electronics* **93**, 100498 (2024).

[6] D. Lujan, J. Choe, M. Rodriguez-Vega, Z. Ye, A. Leonardo, T. N. Nunley, L.-J. Chang, S.-F. Lee, J. Yan, G. A. Fiete, R. He, and X. Li, *Nature Communications* **13**, 2527 (2022).

[7] C. Jin, Z. Tao, K. Kang, K. Watanabe, T. Taniguchi, K. F. Mak, and J. Shan, *Nature Materials* **19**, 1290 (2020).

[8] X.-X. Zhang, S. Jiang, J. Lee, C. Lee, K. F. Mak, and J. Shan, *Nano Letters* **21**, 5045 (2021).

[9] F. Casola, T. van der Sar, and A. Yacoby, *Nature Reviews Materials* **3**, 17088 (2018).

[10] C. Du, T. van der Sar, T. X. Zhou, P. Upadhyaya, F. Casola, H. Zhang, M. C. Onbasli, C. A. Ross, R. L. Walsworth, Y. Tserkovnyak, and A. Yacoby, *Science* **357**, 195 (2017).

[11] S. Hsieh, P. Bhattacharyya, C. Zu, T. Mittiga, T. J. Smart, F. Machado, B. Kobrin, T. O. Höhn, N. Z. Rui, M. Kamrani, S. Chatterjee, S. Choi, M. Zaletel, V. V. Struzhkin, J. E. Moore, V. I. Levitas, R. Jeanloz, and N. Y. Yao, *Science* **366**, 1349 (2019).

[12] T. I. Andersen, B. L. Dwyer, J. D. Sanchez-Yamagishi, J. F. Rodriguez-Nieva, K. Agarwal, K. Watanabe, T. Taniguchi, E. A. Demler, P. Kim, H. Park, and M. D. Lukin, *Science* **364**, 154 (2019).

[13] H. Wang, S. Zhang, N. J. McLaughlin, B. Flebus, M. Huang, Y. Xiao, C. Liu, M. Wu, E. E. Fullerton, Y. Tserkovnyak, and C. R. Du, *Science Advances* **8**, 10.1126/sciadv.abg8562 (2022).

[14] M. Huang, Z. Sun, G. Yan, H. Xie, N. Agarwal, G. Ye, S. H. Sung, H. Lu, J. Zhou, S. Yan, S. Tian, H. Lei, R. Hovden, R. He, H. Wang, L. Zhao, and C. R. Du, *Nature Communications* **14**, 5259 (2023).

[15] F. Machado, E. A. Demler, N. Y. Yao, and S. Chatterjee, *Physical Review Letters* **131**, 070801 (2023).

[16] A. Laraoui, F. Dolde, C. Burk, F. Reinhard, J. Wrachtrup, and C. A. Meriles, *Nature Communications* **4**, 1651 (2013).

[17] T. Staudacher, F. Shi, S. Pezzagna, J. Meijer, J. Du, C. A. Meriles, F. Reinhard, and J. Wrachtrup, *Science* **339**, 561 (2013).

[18] B. Myers, A. Das, M. Dartialih, K. Ohno, D. Awschalom, and A. Bleszynski Jayich, *Physical Review Letters* **113**, 027602 (2014).

[19] T. Rosskopf, A. Dussaux, K. Ohashi, M. Loretz, R. Schirhagl, H. Watanabe, S. Shikata, K. Itoh, and C. Degen, *Physical Review Letters* **112**, 147602 (2014).

[20] E. Schäfer-Nolte, L. Schlipf, M. Ternes, F. Reinhard, K. Kern, and J. Wrachtrup, *Physical Review Letters* **113**, 217204 (2014).

[21] J.-P. Tetienne, A. Lombard, D. A. Simpson, C. Ritchie, J. Lu, P. Mulvaney, and L. C. L. Hollenberg, *Nano Letters* **16**, 326 (2016).

[22] B. L. Dwyer, L. V. Rodgers, E. K. Urbach, D. Bluvstein, S. Sangtawesin, H. Zhou, Y. Nassab, M. Fitzpatrick, Z. Yuan, K. De Greve, E. L. Peterson, H. Knowles, T. Sumarac, J.-P. Chou, A. Gali, V. Dobrovitski, M. D. Lukin, and N. P. de Leon, *PRX Quantum* **3**, 040328 (2022).

[23] E. J. Davis, B. Ye, F. Machado, S. A. Meynell, W. Wu, T. Mittiga, W. Schenken, M. Joos, B. Kobrin, Y. Lyu, Z. Wang, D. Bluvstein, S. Choi, C. Zu, A. C. B. Jayich, and N. Y. Yao, *Nature Physics* **19**, 836 (2023).

[24] R. Xue, N. Maksimovic, P. E. Dolgirev, L.-Q. Xia, R. Kitagawa, A. Müller, F. Machado, D. R. Klein, D. MacNeill, K. Watanabe, T. Taniguchi, P. Jarillo-Herrero, M. D. Lukin, E. Demler, and A. Yacoby, *arXiv e-prints*, arXiv:2403.01057 (2024).

[25] M. E. Ziebel, M. L. Feuer, J. Cox, X. Zhu, C. R. Dean, and X. Roy, *Nano Letters* **24**, 4319 (2024).

[26] S. A. López-Paz, Z. Guguchia, V. Y. Pomjakushin, C. Witteveen, A. Cervellino, H. Luetkens, N. Casati, A. F. Morpurgo, and F. O. von Rohr, *Nature Communications* **13**, 4745 (2022).

[27] E. J. Telford, A. H. Dismukes, R. L. Dudley, R. A. Wiscons, K. Lee, D. G. Chica, M. E. Ziebel, M.-G. Han, J. Yu, S. Shabani, A. Scheie, K. Watanabe, T. Taniguchi, D. Xiao, Y. Zhu, A. N. Pasupathy, C. Nuckolls, X. Zhu, C. R. Dean, and X. Roy, *Nature Materials* **21**, 754 (2022).

[28] K. Lee, A. H. Dismukes, E. J. Telford, R. A. Wiscons, J. Wang, X. Xu, C. Nuckolls, C. R. Dean, X. Roy, and X. Zhu, *Nano Letters* **21**, 3511 (2021).

[29] A. Scheie, M. Ziebel, D. G. Chica, Y. J. Bae, X. Wang, A. I. Kolesnikov, X. Zhu, and X. Roy, *Advanced Science* **9**, 10.1002/advs.202202467 (2022).

[30] D. J. Rizzo, A. S. McLeod, C. Carnahan, E. J. Telford, A. H. Dismukes, R. A. Wiscons, Y. Dong, C. Nuckolls, C. R. Dean, A. N. Pasupathy, X. Roy, D. Xiao, and D. N. Basov, *Advanced Materials* **34**, 2201000 (2022).

[31] M. A. Tschudin, D. A. Broadway, P. Reiser, C. Schrader, E. J. Telford, B. Gross, J. Cox, A. E. E. Dubois, D. G. Chica, R. Rama-Eiroa, E. J. G. Santos, M. Poggio, M. E. Ziebel, C. R. Dean, X. Roy, and P. Maletinsky, *arXiv e-prints*, arXiv:2312.09279 (2023).

[32] Here the stray field is defined as $B_{stray} = B - B_{avg}$, where the subtraction of the signal averaged over all pixels in the image (B_{avg}) approximately removes the constant offset due to the external bias field [48].

[33] T. S. Ghiasi, M. Borst, S. Kurdi, B. G. Simon, I. Bertelli, C. Boix-Constant, S. Mañas-Valero, H. S. J. van der Zant, and T. van der Sar, *npj 2D Materials and Applications* **7**, 62 (2023).

[34] We note that similar normalization procedures to quantify a relative change in decoherence signal are used for other NV sensing techniques, e.g. DEER [22].

[35] Note that $\tau = T_2$ corresponds to the time at which the coherence signal has decayed to a fixed value of $C(T_2) = e^{-2}$, allowing for a fair comparison of the decoherence rate across coherence decays with different functional forms.

[36] T. M. J. Cham, S. Karimeddiny, A. H. Dismukes, X. Roy, D. C. Ralph, and Y. K. Luo, *Nano Letters* **22**, 6716 (2022).

[37] B. I. Halperin and P. C. Hohenberg, *Physical Review*

177, 952 (1969).

[38] The $\langle \phi^2(\tau) \rangle_{T_{Norm}}^{ens}$ data and model in Figure 4a are normalized using a reference temperature near criticality ($T_{Ref} = 136.75$ K), as we expect the mean-field derived structure function (Eq (5)) to describe fluctuations quantitatively only for a range of temperatures near criticality.

[39] Y. Sun, F. Meng, C. Lee, A. Soll, H. Zhang, R. Ramesh, J. Yao, Z. Sofer, and J. Orenstein, *Nature Physics* **10**, 1038/s41567-024-02387-2 (2024).

[40] Y. J. Bae, J. Wang, A. Scheie, J. Xu, D. G. Chica, G. M. Diederich, J. Cenker, M. E. Ziebel, Y. Bai, H. Ren, C. R. Dean, M. Delor, X. Xu, X. Roy, A. D. Kent, and X. Zhu, *Nature* **609**, 282 (2022).

[41] K. Yang, G. Wang, L. Liu, D. Lu, and H. Wu, *Physical Review B* **104**, 144416 (2021).

[42] N. Defenu, T. Donner, T. Macrì, G. Pagano, S. Ruffo, and A. Trombettoni, *Reviews of Modern Physics* **95**, 035002 (2023).

[43] B. Sbierski, M. Bintz, S. Chatterjee, M. Schuler, N. Y. Yao, and L. Pollet, *Physical Review B* **109**, 144411 (2024).

[44] b is typically a non-universal $O(1)$ constant in the range of $\sim 0.1 - 5$ [49, 50].

[45] J. M. Kosterlitz, *Journal of Physics C: Solid State Physics* **7**, 1046 (1974).

[46] J. V. José, L. P. Kadanoff, S. Kirkpatrick, and D. R. Nelson, *Physical Review B* **16**, 1217 (1977).

[47] J. Rovny, Z. Yuan, M. Fitzpatrick, A. I. Abdalla, L. Futamura, C. Fox, M. C. Cambria, S. Kolkowitz, and N. P. de Leon, *Science* **378**, 1301 (2022).

[48] Z. Kazi, I. M. Shelby, H. Watanabe, K. M. Itoh, V. Shuttanandan, P. A. Wiggins, and K.-M. C. Fu, *Physical Review Applied* **15**, 054032 (2021).

[49] L. Vanderstraeten, B. Vanhecke, A. M. Läuchli, and F. Verstraete, *Physical Review E* **100**, 062136 (2019).

[50] M. M. Rams, P. Czarnik, and L. Cincio, *Physical Review X* **8**, 041033 (2018).

[51] S. Sangtawesin, B. L. Dwyer, S. Srinivasan, J. J. Allred, L. V. Rodgers, K. De Greve, A. Stacey, N. Dontschuk, K. M. O'Donnell, D. Hu, D. A. Evans, C. Jaye, D. A. Fischer, M. L. Markham, D. J. Twitchen, H. Park, M. D. Lukin, and N. P. de Leon, *Physical Review X* **9**, 031052 (2019).

[52] S. T. Alsid, J. F. Barry, L. M. Pham, J. M. Schloss, M. F. O'Keeffe, P. Cappellaro, and D. A. Braje, *Physical Review Applied* **12**, 044003 (2019).

[53] M. Posselt and J. Biersack, *Nuclear Instruments and Methods in Physics Research Section B: Beam Interactions with Materials and Atoms* **64**, 706 (1992).

[54] N. Raatz, C. Scheuner, S. Pezzagna, and J. Meijer, *physica status solidi (a)* **216**, 10.1002/pssa.201900528 (2019).

[55] E. Bauch, S. Singh, J. Lee, C. A. Hart, J. M. Schloss, M. J. Turner, J. F. Barry, L. M. Pham, N. Bar-Gill, S. F. Yelin, and R. L. Walsworth, *Physical Review B* **102**, 134210 (2020).

[56] L. Wang, I. Meric, P. Y. Huang, Q. Gao, Y. Gao, H. Tran, T. Taniguchi, K. Watanabe, L. M. Campos, D. A. Muller, J. Guo, P. Kim, J. Hone, K. L. Shepard, and C. R. Dean, *Science* **342**, 614 (2013).

[57] D. B. Bucher, D. P. L. Aude Craik, M. P. Backlund, M. J. Turner, O. Ben Dor, D. R. Glenn, and R. L. Walsworth, *Nature Protocols* **14**, 2707 (2019).

[58] D. B. Durham, D. F. Ogletree, and E. S. Barnard, *Surface and Interface Analysis* **50**, 1174 (2018).

[59] C. S. Aitchison, R. Davies, I. D. Higgins, S. R. Longley, B. H. Newton, J. F. Wells, and J. C. Williams, *IEEE Transactions on Microwave Theory and Techniques* **19**, 928 (1971).

[60] K. Gupta, R. Garg, and R. Chadha, *Computer-Aided Design of Microwave Circuits* (Artech House, Inc., Dedham, MA, 1981).

[61] J. R. Rabreau, P. Reichart, G. Tamanyan, D. N. Jamieson, S. Prawer, F. Jelezko, T. Gaebel, I. Popa, M. Domhan, and J. Wrachtrup, *Applied Physics Letters* **88**, 10.1063/1.2158700 (2006).

[62] S. van der Walt, J. L. Schönberger, J. Nunez-Iglesias, F. Boulogne, J. D. Warner, N. Yager, E. Gouillart, and T. Yu, *PeerJ* **2**, e453 (2014).

[63] M. Ortner and L. G. Coliado Bandeira, *SoftwareX* **11**, 100466 (2020).

[64] A. Dréau, M. Lesik, L. Rondin, P. Spinicelli, O. Arcizet, J.-F. Roch, and V. Jacques, *Physical Review B* **84**, 195204 (2011).

[65] J. F. Barry, J. M. Schloss, E. Bauch, M. J. Turner, C. A. Hart, L. M. Pham, and R. L. Walsworth, *Reviews of Modern Physics* **92**, 015004 (2020).

[66] A. Schweiger and G. Jeschke, *Principles of Pulse Electron Paramagnetic Resonance* (Oxford University Press, New York, 2001).

[67] D. Puzzuoli, C. J. Wood, D. J. Egger, B. Rosand, and K. Ueda, *Journal of Open Source Software* **8**, 5853 (2023).

Supplementary Information: Quantum Noise Spectroscopy of Critical Slowing Down in an Atomically Thin Magnet

CONTENTS

References	8
I. Sample Preparation	11
A. NV Ensemble Preparation and Characterization	11
1. C-TRIM Depth Distribution Simulation	12
2. NV Ensemble Spin Coherence	13
B. CrSBr Exfoliation and Transfer	14
II. Experimental Details	14
A. Confocal ODMR Setup	14
B. Microwave Delivery	16
C. Pulse Sequences	17
1. Contrast Definitions	18
D. Magnetometry	18
E. Sample Drift Correction	18
III. CrSBr Magnetic Simulations	20
IV. Temperature Range of Spin Echo Normalization	21
V. Critical Dynamics Analysis	25
A. Simulation Methods and Definitions	25
B. Fit Comparisons	26
C. Effects of the NV Ensemble Depth Distribution on Decoherence Dynamics	27

I. SAMPLE PREPARATION

A. NV Ensemble Preparation and Characterization

A [100]-oriented electronic grade diamond substrate with a $\sim 2\mu\text{m}$ thick isotopically pure ^{12}C overgrown diamond layer was purchased from QuantumDiamonds, GmbH. The as-received diamond was cleaned by ultrasonication followed by tri-acid cleaning in a boiling mixture of 1:1:1 perchloric:nitric:sulfuric acid refluxing for 2 hours. The ^{12}C surface was then implanted with $^{15}\text{N}^+$ ions with 25 keV implantation energy, $2 \times 10^{12} \text{ cm}^{-2}$ dose, and 5° sample tilt (Coherent, Inc., Innovion Corp., San Jose, CA). After ion implantation, the sample was cleaned with the tri-acid procedure and evaluated for surface contamination using XPS. The diamond was then annealed under vacuum ($< 1 \times 10^{-5} \text{ Torr}$) using the ramped annealing procedure reported by Sangtawesin *et al.* [51] without the 1200°C step, followed by tri-acid cleaning. The sample was then annealed under O_2 gas at 455°C following the procedure in Sangtawesin *et al.* [51] in order to form an oxygen terminated surface to stabilize the NV^- charge state for NVs formed at shallow depths within the implanted ^{15}N distribution (Figure S1). Following O_2 annealing the diamond was cleaned with a 1:2 hydrogen peroxide:sulfuric acid piranha solution. In between steps the diamond could be sonicated with Milli-Q water followed by sonication in electronic grade 2-propanol (Sigma Aldrich, 733458). A C-TRIM simulation for the estimated ^{15}N ion depth distribution is shown in Figure S2.

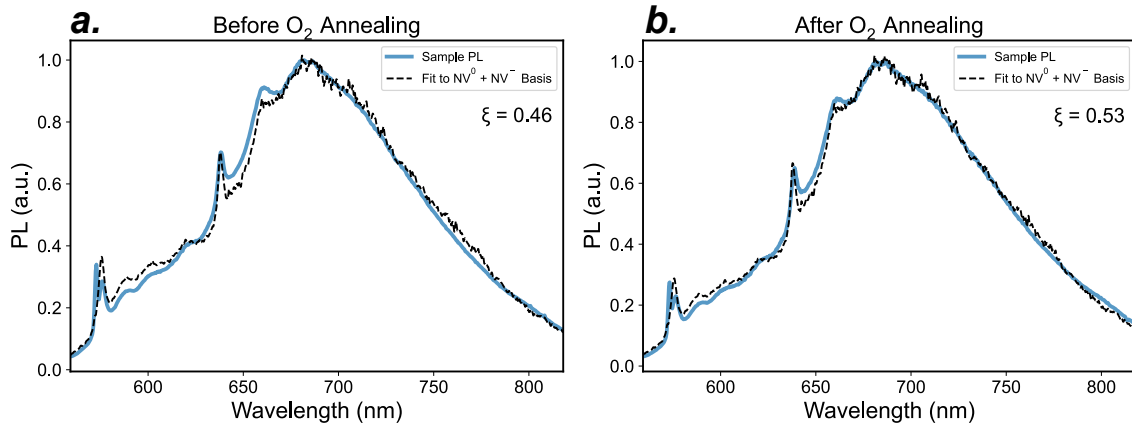


FIG. S1. We determined the NV^- to NV^0 ratio before and after the O_2 annealing steps of our sample preparation using the photoluminescence decomposition method of Alsid *et al.* [52]. Photoluminescence spectra were measured on a confocal fluorescence set up using $\sim 1.8\text{mW}$ 532 nm CW laser excitation focused onto the sample with a 0.6 NA objective (Olympus LUCPlanFL N, 40x). Dichroic and longpass filters were used to filter the laser excitation and the fluorescence spectra were recorded with a spectrograph (Acton SP2300i) and CCD camera (Princeton Instruments Pixis 400BRX). The data were intensity corrected by measuring the spectrum of a calibrated tungsten halogen light source (StellarNet SL1-CAL). The fraction of the total NV yield in the NV^- charge state (ξ) was determined by fitting the spectra to a sum of basis functions c_- and c_0 (corresponding to the emission spectra of NV^- and NV^0 , respectively), and weighting c_0 by a factor κ_{532} corresponding to the difference in emission rate between the NV^- and NV^0 charge states excited at 532 nm, using the equation: $\xi = \frac{[\text{NV}^-]}{[\text{NV}^-] + [\text{NV}^0]} = \frac{c_-}{c_- + \kappa_{532}c_0}$ [52]. O_2 annealing was found to improve the total NV^- fraction by a factor of $\sim 15\%$ ($\xi = 0.46$ before O_2 annealing to $\xi = 0.53$ after O_2 annealing).

1. *C-TRIM Depth Distribution Simulation*

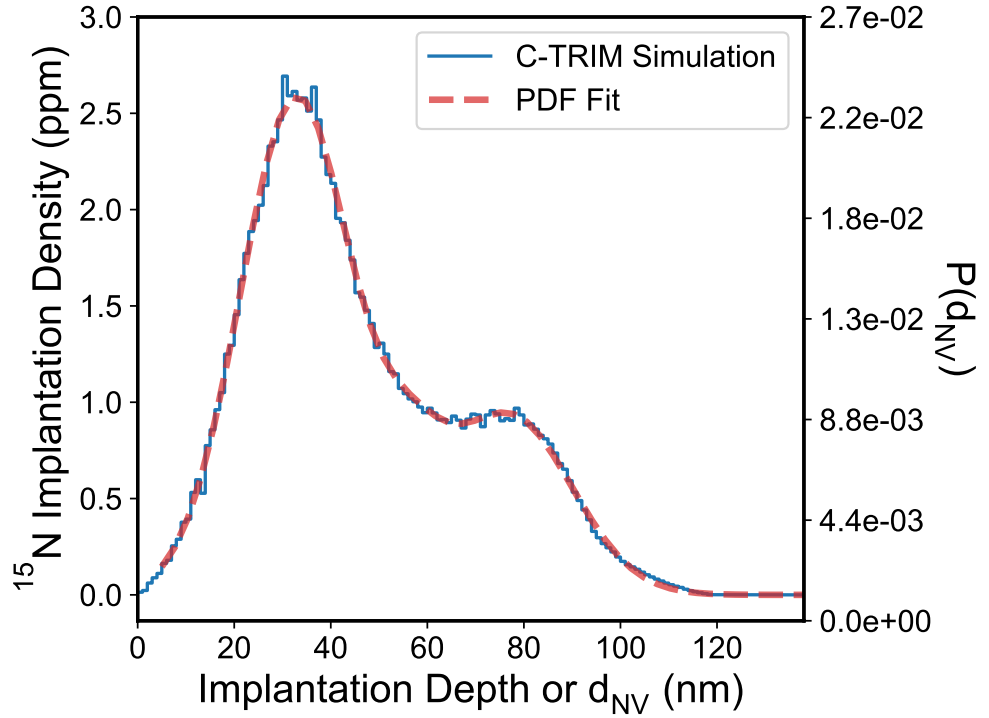


FIG. S2. We modelled the ^{15}N (and NV) depth distribution by performing C-TRIM[53, 54] simulations for $25keV$ $^{15}N^+$ ion implantation into [100] oriented diamond. C-TRIM was used (as opposed to SRIM) to model the tail of the ion distribution at larger depths due to ion channelling [54]. Based on the parameters determined by Raatz *et al.*[54] we used a value of $C_{el} = 1.715$ for an implantation energy of $25keV$. We additionally simulated surface roughness by adding a $3nm$ thick amorphous carbon layer with the density of diamond ($3.51g/cm^3$)[54]. Simulations were performed for a tilt angle of 2° to compensate for the $\sim 3^\circ$ miscut angle of our diamond sample. The left axis shows the simulated ^{15}N implantation density in ppm. We also fit the C-TRIM simulation to a sum of three truncated Gaussians, which was then normalized to an area of 1 to model an estimated probability density function $P(d_{NV})$ for the NV depth d_{NV} (right axis). From the first moment of $P(d_{NV})$ we determine a mean NV depth $\langle d_{NV} \rangle = 46.6\text{ nm}$.

2. NV Ensemble Spin Coherence

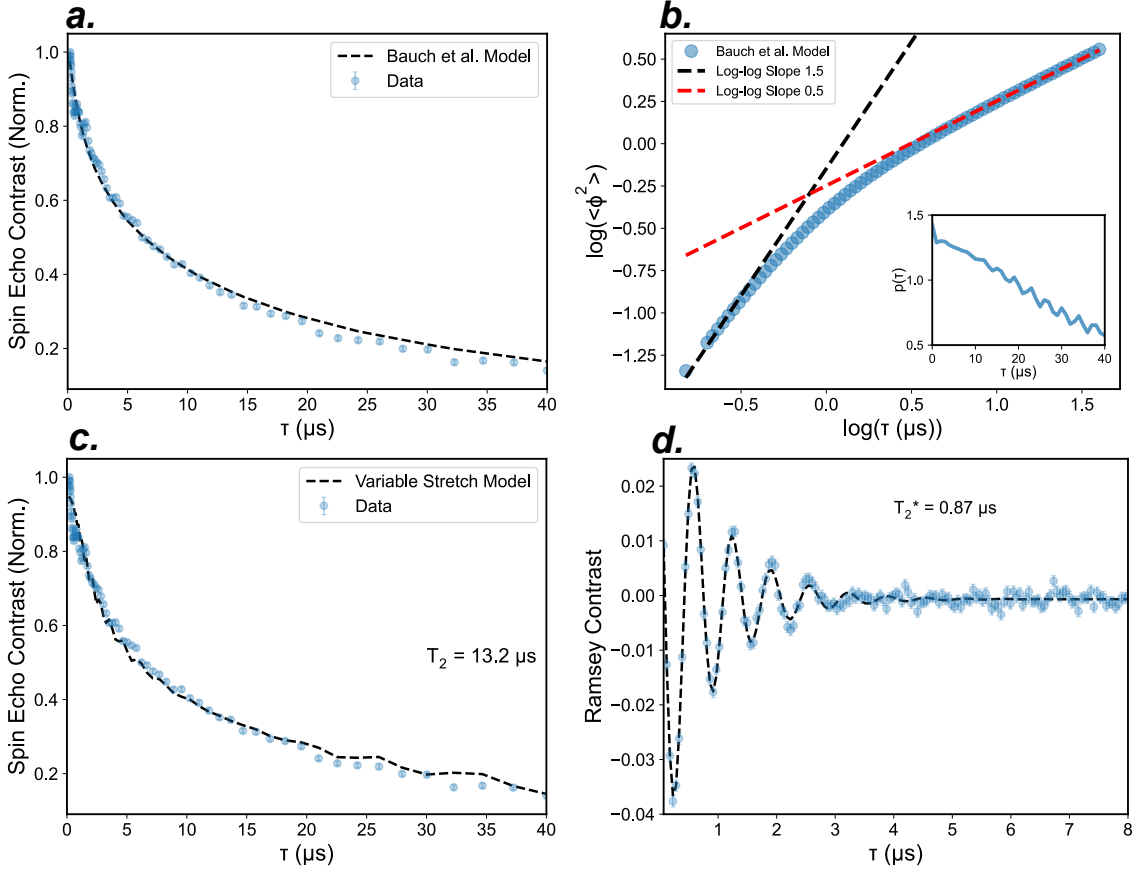


FIG. S3. To characterize the spin coherence properties of the NV ensemble we measured T_2 using spin echo and T_2^* using Ramsey on a position $\sim 1 \mu\text{m}$ off of the flake at $\sim 137.5 \text{ K}$. To compare the results with models for NV ensemble coherence, we first fit the spin echo coherence decay by numerically solving the ensemble averaged coherence model from Bauch *et al.* [55]. Here, the coherence decay for a single NV undergoing decoherence from the diamond spin bath is defined as $C(\tau) = e^{-\chi_{SE}(\tau)}$, with $\chi_{SE}(\tau) = \Delta_{single}^2 \tau_c^2 \left[\frac{\tau}{\tau_c} - 3 - e^{-\tau/\tau_c} + 4e^{-\tau/2\tau_c} \right]$ where Δ_{single}^2 determines the coupling strength to fluctuations from the diamond spin bath which have a characteristic fluctuation correlation time τ_c [55]. The coherence for an NV ensemble is obtained by solving $C_{ens}(\tau) = \iint e^{-\chi_{SE}(\tau)} P(\Delta_{single}) P(\tau_c) d\Delta_{single} d\tau_c$ where $P(\Delta_{single})$ is a probability distribution function for Δ_{single} characterized by a shape parameter Δ_{ens} and $P(\tau_c)$ is a probability distribution for τ_c with shape parameters $\tau_{c,ens}$ and λ [55]. The plot in (a) shows the measured spin echo coherence $C(\tau)$ and best fit to the model with $\Delta_{ens} = 0.4 \text{ MHz}$, $\tau_{c,ens} = 0.5 \mu\text{s}$, and $\lambda = 3.57$. Defining $C(\tau) = e^{-\langle\phi^2(\tau)\rangle/2}$ as in the main text, we then evaluate the power law behavior of $\langle\phi^2(\tau)\rangle$ from the model for $C_{ens}(\tau)$ by plotting $\langle\phi^2\rangle$ vs τ on a log-log scale in (b). Linear fitting of the early and late time log-log behavior of $\langle\phi^2\rangle$ vs τ recovers the expected $3/2$ and $1/2$ power law behavior for $\tau < \tau_{c,ens}$ and $\tau > \tau_{c,ens}$ respectively for a 3D spin bath [23]. To determine T_2 we fit the coherence decay to a function $C(\tau) = e^{-\frac{\tau}{T_2} p(\tau)}$ where we input a τ dependent variation in the stretch parameter $p(\tau)$ which is determined by calculating the derivative of $\log(\langle\phi^2\rangle)$ vs $\log(\tau)$ from (b) ($p(\tau)$ is shown in the inset of (b)). A fit of the data to $e^{-\frac{\tau}{T_2} p(\tau)}$ is shown in (c), from which we determine $T_2 = 13.2 \mu\text{s}$. Based on the results of Bauch *et al.* [55] we would expect T_2 in the range of 10's of μs for a bulk NV ensemble formed from 2.5 ppm nitrogen density. We suspect that due to the spread of NV depths near the surface in our ensemble (Fig S2) there is likely additional interaction between the NV ensemble and a surface spin bath (with possible additional contributions of surface spin noise due residual polymer from the CrSBr transfer), which reduces T_2 . We also measured T_2^* using a $\frac{\pi}{2}_{(x)} \rightarrow \frac{\pi}{2}_{(x,-x)}$ Ramsey pulse sequence (see Section IIC). We fit the data to a function of the form $C_{Ramsey}(\tau) \propto e^{-(\tau/T_2^*)} \cos(\omega_R \tau)$, where ω_R is the Ramsey interference frequency (d). From the fits to the Ramsey data we obtain $T_2^* = 0.87 \mu\text{s}$.

B. CrSBr Exfoliation and Transfer

Bulk crystals of CrSBr were synthesized using a chemical vapor transport reaction with a temperature gradient of 950°C to 850°C as described in detail in reference [29]. Few-layer flakes of CrSBr were prepared by Scotch tape exfoliation from a bulk CrSBr crystal onto SiO_2 (285 nm)/Si wafers. The thickness of the flakes were determined using atomic force microscopy and correlated optical contrast [27]. Transfer of CrSBr flakes onto the diamond substrate was performed using a standard dry stamp method [56] with polycarbonate (PC) as the pick up polymer. The substrate was oriented on a rotation stage such that the long axis of the CrSBr flake of interest was aligned roughly parallel with a [110] edge of the diamond substrate as seen under the microscope camera prior to transfer. Following transfer the PC was washed off from the diamond with chloroform.

II. EXPERIMENTAL DETAILS

A. Confocal ODMR Setup

All experiments were performed on a home-built laser scanning confocal optically detected magnetic resonance (ODMR) microscope built around a Janis ST-500 optical cryostat (Figure S3). A 532 nm laser (Coherent Sapphire SF 532-50) is sent through an acousto-optic modulator (Isomet M1205-P80L-1) in a double-pass configuration for pulse modulation and directed via a 550 nm longpass dichroic mirror (Thorlabs DMLP550R) to a set of galvo-mirrors (Thorlabs GVS002) positioned in the back focal plane of the scan lens (Thorlabs SL50-CLS2) in a $4f$ imaging system, where a tube lens (Thorlabs TTL200-S8) and a microscope objective (Nikon Plan Fluor 60x, 0.7NA) image the scanning laser spot onto the sample. Typical CW laser power on the sample is $\sim 1 \text{ mW}$. Photoluminescence (PL) from the sample is spectrally filtered with a 550 nm longpass dichroic mirror and additional 650 nm longpass filters, after which it is spatially filtered with $30 \mu\text{m}$ pinhole. The PL is then split by a 850 nm dichroic mirror to separate NV PL (in the range of 650-850 nm) from the CrSBr PL at $\sim 930 \text{ nm}$. The NV PL is sent to a fiber coupled single photon counting APD (Excelitas SPCM-AQRH-15-FC), and the CrSBr PL is sent to a superconducting nanowire single photon detector (Single Quantum EOS-6). Photon counts from the detectors are read out using gated counter channels on a DAQ (NI USB-6343). Microwave delivery was achieved by mounting the diamond onto a PCB resonator, where a Ω -loop planar inductor delivered homogeneous RF magnetic fields over an area around $\sim 0.5 \text{ mm}^2$ (see Section II B for details). The diamond was positioned on the PCB under a microscope such that the CrSBr flake was near the center of the Ω -loop. The diamond was silver pasted onto the PCB and positioned such that it contacted cooling pads connected by vias to the ground plane of the PCB which is in thermal contact with the cold finger of the cryostat (see Section II B). Microwaves are sourced from a signal generator (Stanford Research Systems SG384/3) and passed through a gated RF switch (MiniCircuits ZASWA-2-50DRA+) to generate pulses. Microwave pulses are then sent through an amplifier (MiniCircuits ZHL-16W-43-S+) and sent to the PCB. The output of the amplifier is protected with a circulator (DiTom D3C2040). Phase modulation of the microwave pulses is achieved by sending input signals (generated by gating a DC voltage with MiniCircuits ZASWA-2-50DRA+ switches) to the IQ modulator built into the SG384/3 [57]. A PulseBlaster ESR-Pro-500 pulse generator is programmed to deliver TTL pulses through output channels to control modulation of the AOM, gating of microwave switches, and gating of DAQ counter channels (see Section II C). Two 3" OD ring magnets (K&J Magnetics RZ0Y0X0) are mounted in a coaxial configuration outside the cryostat on a 5-axis stage and are adjusted such that a $\sim 3.5 \text{ mT}$ bias field is aligned along a [111] axis of the diamond (see Section II D). The cryostat is cooled with a closed cycle Helium recirculating system (Janis RGC4) and the temperature is maintained using a PID temperature controller (Lakeshore 335). All instruments and experiments are controlled using custom written Python code with the ScopeFoundry platform [58].

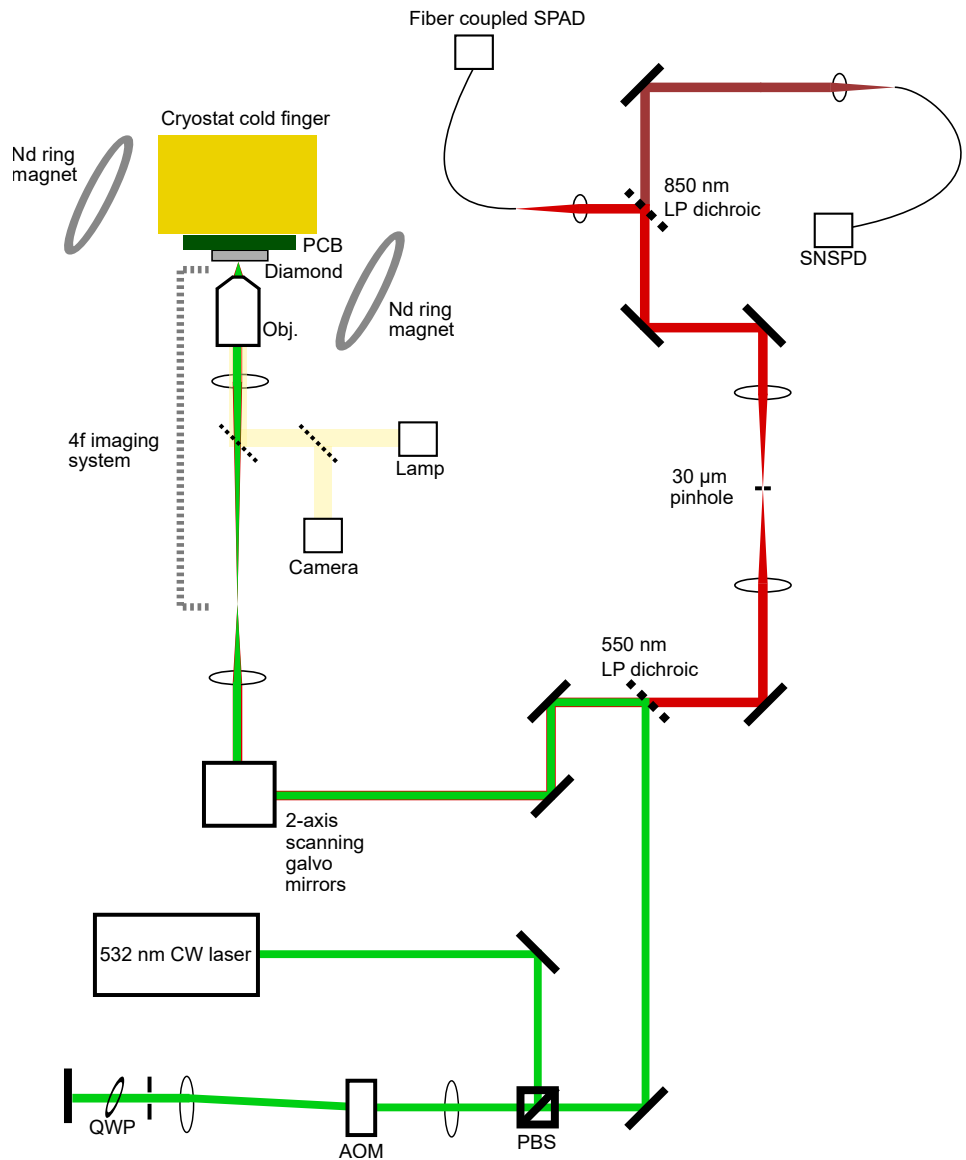


FIG. S4. Diagram of the confocal ODMR setup used in this work.

B. Microwave Delivery

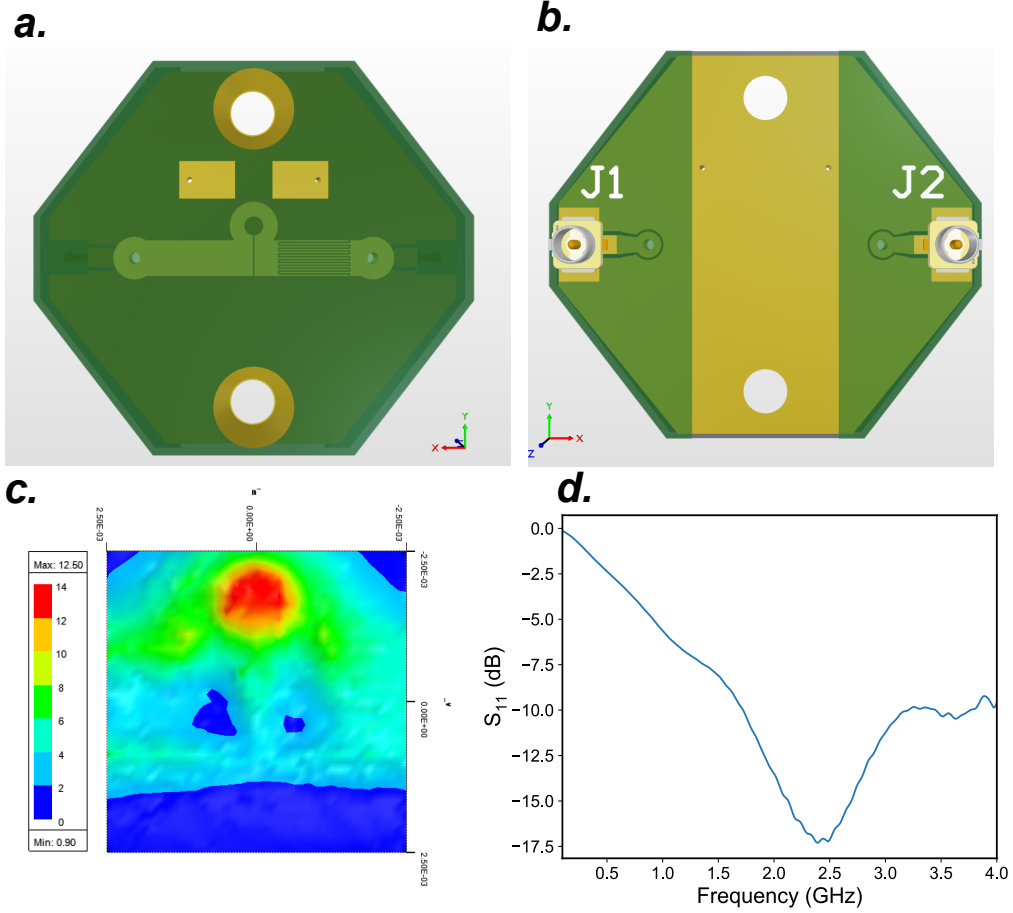


FIG. S5. For microwave delivery we designed a planar 50-Ohm transmission-line microstrip LC resonator consisting of a Ω -loop planar inductor in series with an interdigitated planar capacitor[59, 60] fabricated onto a PCB (top view in (a), bottom view in (b)). The transmission line is terminated with a 50 Ohm resistor connected to J1 (shown in (b)) via a 50 Ohm coax cable, such that the impedance at the LC resonance frequency is 50 Ohms. The microstrip width and dimensions of the planar Ω -loop inductor and interdigitated capacitor were determined by optimizing the simulated S_{11} in HFSS (Ansys) to obtain a broad LC resonance centered around ~ 2.7 GHz matched to an input impedance of 50 Ohms. In (c) we show a HFSS simulation of the H-field near resonance at the surface of a 0.3mm thick diamond placed on top of the PCB, where we achieve a $\sim 0.5mm^2$ area of uniform maximum H-field above the center of the Ω -loop. In cryogenic experiments, an area of the ground plane not covered with solder mask (large gold rectangular area at the center of the PCB in (b)) is mounted directly onto the cold finger of the cryostat contacted with silver paste. The ground plane is connected to two cooling pads through vias (gold rectangular areas above the Ω -loop in (a)), which contact the diamond mounted on the top side of the PCB. In (d) we show S_{11} measured with a VNA (Agilent N5230A / N4431-60003) on a 50-Ohm terminated PCB manufactured from our design, which shows a broad LC resonance near 2.5 GHz.

C. Pulse Sequences

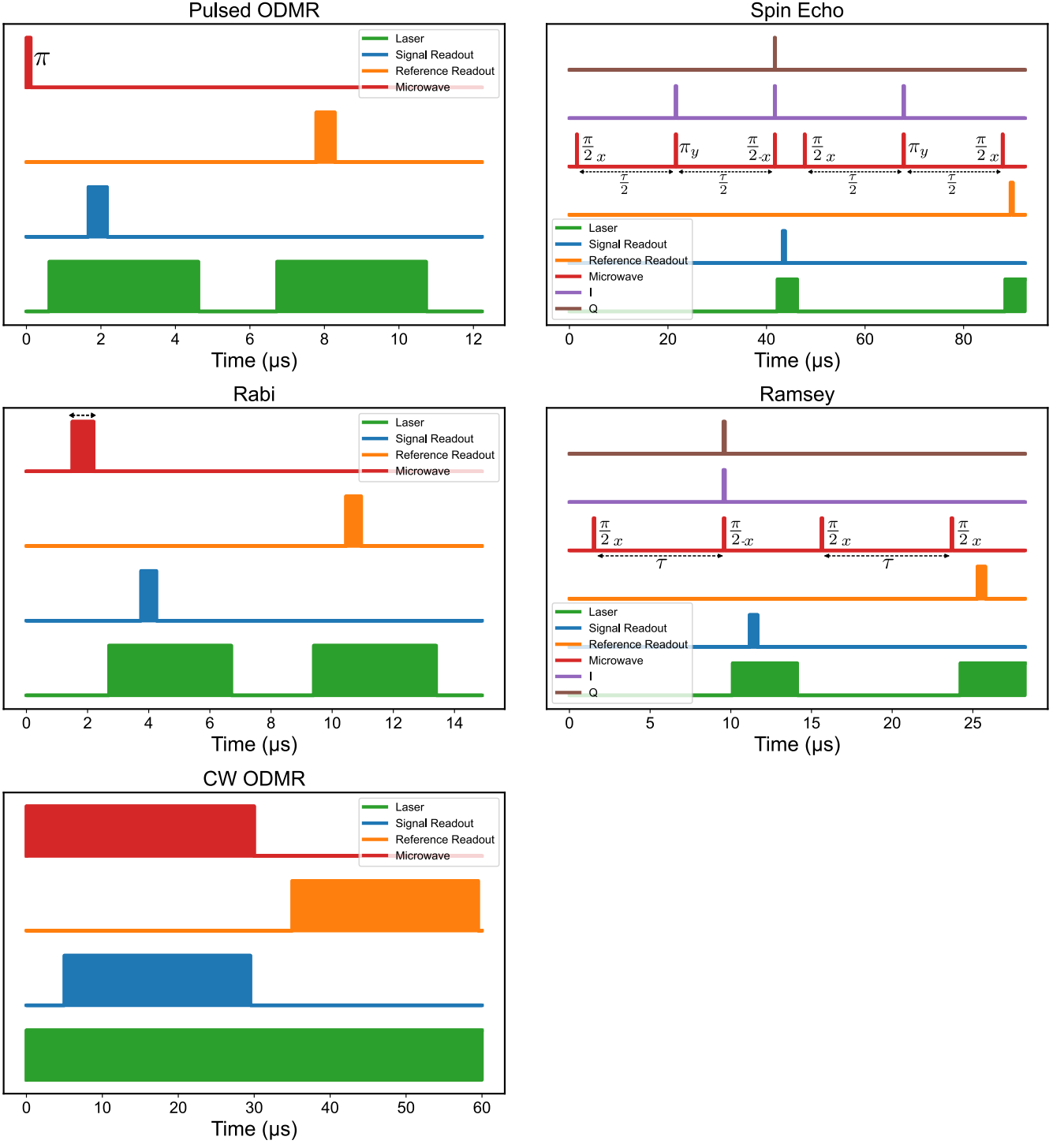


FIG. S6. Here we show the timing sequences for the TTL pulse outputs from channels of the PulseBlaster which control digital modulation of the AOM (labeled "Laser"), gating of the RF switch that feeds the microwave amplifier from the SG384/3 signal generator (labeled "Microwave"), gating of DAQ counter channels for signal and reference readout of the APD (labeled "Signal Readout" and "Reference Readout"), and gating of RF switches which feed a DC voltage into the I and Q modulation inputs of the SG384/3 signal generator (labeled "I" and "Q"). For pulsed ODMR, spin echo, Rabi, and Ramsey, the signal and reference readout pulses are set to 500ns and laser pulses are set to a duration of 4μs. A delay between the laser pulse onset and the signal and readout pulses is set to compensate for an electronic delay from the instruments [57]. The I and Q modulation pulses are padded by 20ns with respect to the π and $\pi/2$ pulses in spin echo and Ramsey to compensate for the response time of the switches and SG384/3 IQ modulation [57].

1. Contrast Definitions

For pulsed ODMR, Rabi and CW ODMR experiments, the raw contrast is defined as $\frac{\text{Signal}-\text{Reference}}{\text{Reference}}$ ("signal" and "reference" corresponding to data from the readout channels of the DAQ). For spin echo (or Ramsey) experiments raw contrast is defined as $2\frac{\text{Signal}-\text{Reference}}{\text{Signal}+\text{Reference}}$ [57].

D. Magnetometry

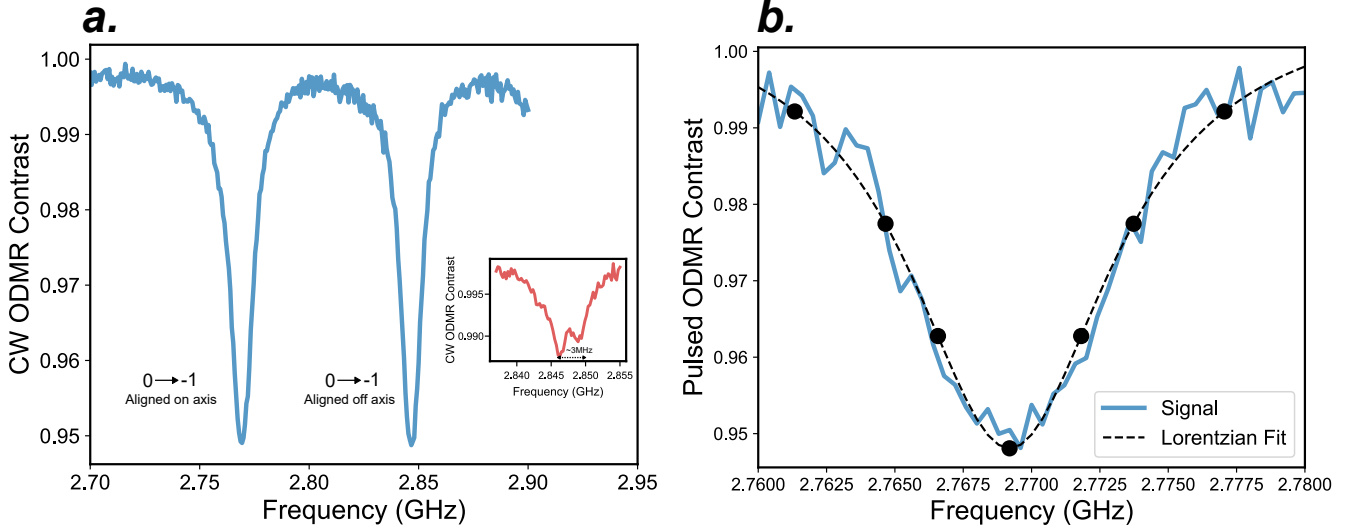


FIG. S7. For all AC and DC magnetometry measurements the bias magnetic field is aligned such that the B-field direction is projected along one of the four possible [111] directions of diamond, corresponding to the spin quantization axis of one of four possible subsets of NV orientations in the ensemble [57]. (a) shows the CW ODMR spectrum representing a typical magnetic field alignment. The field is aligned so that the ODMR spectra for the three "off axis" NV orientations (orientations which have the the magnetic field projected partially off-axis from the spin quantization axis) collapse onto one peak with the ~ 3 MHz ^{15}N hyperfine splitting [61] overlapped when measured with low microwave power (inset of (a)). Rabi measurements (Figure S11 d) are then performed at the $|\text{m}_s = 0\rangle \rightarrow |\text{m}_s = -1\rangle$ resonance frequency for the "on axis" NV orientation to determine the $\pi-$ pulse duration for all subsequent coherent pulsed experiments . For pulsed ODMR imaging experiments, seven frequency points are measured which correspond to zero-crossings of 1st, 2nd, 3rd and 4th derivatives of a Lorentzian fit determined from a spectrum initially measured at a position $\sim 1\mu\text{m}$ away from the flake (b). These seven points correspond to the main points of curvature of a Lorentzian function which allows us to fit the pulsed ODMR data measured at each pixel to a full Lorentzian function to create images both of the resonance frequency and pulsed ODMR contrast (see Section V).

E. Sample Drift Correction

In pulsed ODMR imaging experiments, the average count rate from the SNSPD (which records PL from CrSBr) is recorded at each pixel along with the data from the pulsed ODMR pulse sequence (Fig S5), such that PL images of the CrSBr flake and pulsed ODMR images can be constructed from data recorded simultaneously. Typically 460 pixels are recorded for each image with 5000 pulsed ODMR averages per pixel (averaging 1.6 s/pixel and a total of $\sim 12\text{ min}/\text{image}$), and > 20 images are recorded which amounts to a total of $> 1\text{e}5$ pulsed ODMR averages per pixel. Over the course of a several hour measurement, the image will drift slowly (over 10's of minutes) on the scale of 100's of nm to $\sim \mu\text{m}$, which is found to be correlated with thermal fluctuations in the room and is likely due to thermal drift of the optics. This drift is corrected in image post processing by cross correlating the first CrSBr PL image recorded in the measurement sequence with each image in subsequent sequences. The drift is calculated with sub-pixel accuracy using the SCIKIT-IMAGE phase cross correlation routine[62] and is determined as a function of time using the image file timestamps. Image interpolation is then used to correct pixel assignments for images recorded at different times in the measurement and reconstruct drift corrected PL and pulsed ODMR images.

For spin echo experiments drift correction is performed on the fly so that a fixed measurement position on the sample is maintained over long measurement periods. An initial PL image of the CrSBr flake is recorded and position

coordinates on the PL image to perform spin echo measurements are selected. A series of spin echo pulse sequences (typically $1e5$) for 75 different interpulse delay times ($\frac{\tau}{2}$) are then performed at the given coordinates which takes $\sim 6 - 7 \text{ min}$. Another PL image is then measured and cross-correlated with the initial PL image to determine the sample drift and the target coordinates for the next series of spin echo measurements are updated to correct for drift. The process is repeated 75 – 100 times for a total of $1e6 - 1e7$ averages of the spin echo pulse sequence. The typical spread of coordinates sampled over the total course of spin echo measurements (with variation due to differences in the results of image cross correlation) is shown by the red dots in Fig S8 below.

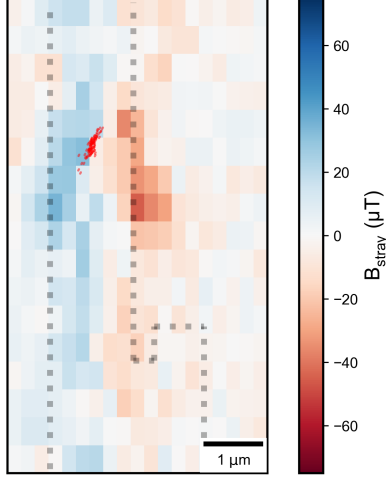


FIG. S8. Pulsed ODMR stray field image recorded at 137.5 K overlaid with the spread of points sampled in spin echo measurements at this temperature.

III. CrSBr MAGNETIC SIMULATIONS

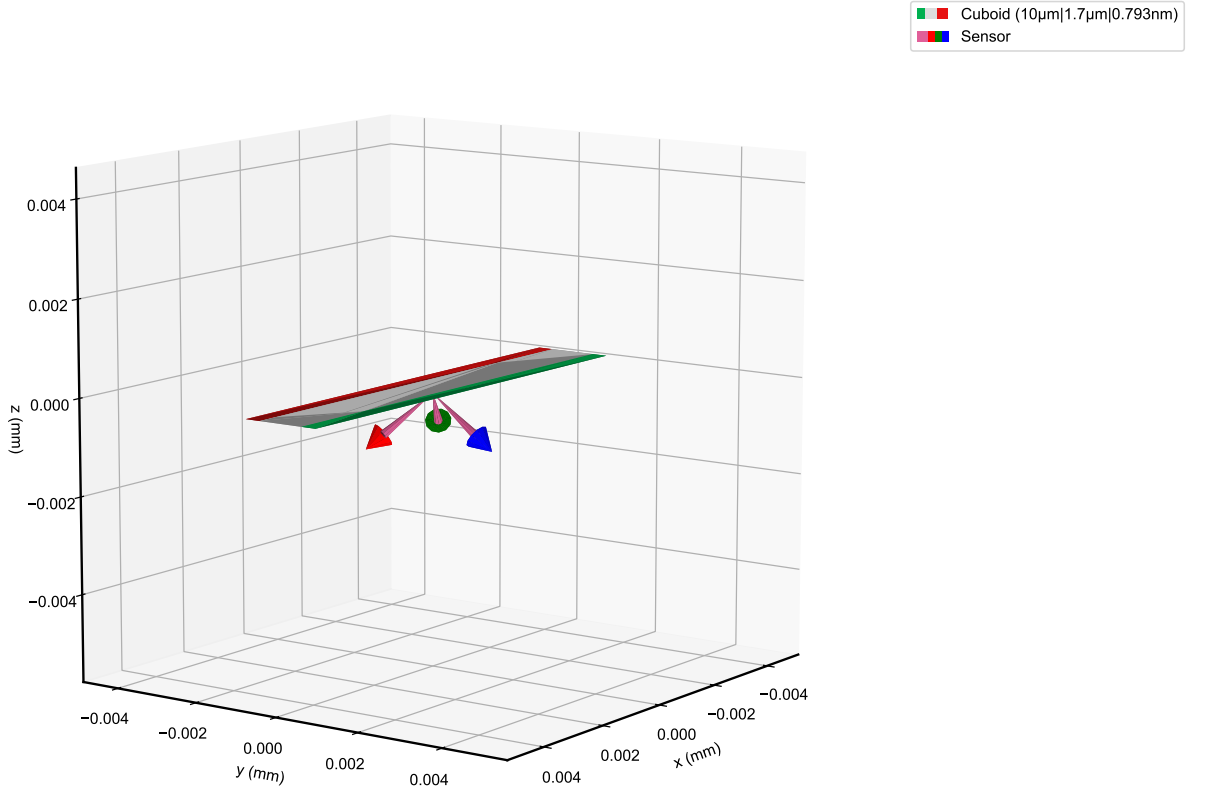


FIG. S9. We used MAGPYLIB [63] to simulate the stray magnetic fields from one uncompensated ferromagnetic monolayer of CrSBr. The geometry of the simulation set up is shown above. We defined the CrSBr flake as a cuboid with x,y dimensions of $10\mu\text{m} \times 1.7\mu\text{m}$ and a z dimension of 0.793nm corresponding to the thickness of one monolayer of CrSBr [26]. The magnetization vector is oriented along y axis and its magnitude (the remanence) is calculated from the CrSBr unit cell magnetization at 100 K reported by López-Paz *et al.* [26] with the CrSBr unit cell volume. Experimentally, the CrSBr flake was oriented roughly so that the rectangular edges of the flake were parallel with the square edges of the diamond substrate during the transfer process such that x and y axes of the flake in the simulation are taken to point along [110] directions of the diamond unit cell, while the z axis corresponds to the [100] direction. We rotate the sensor coordinate system in the simulation such that the z-axis of the sensor (blue arrow in the figure above) in the new coordinate system points in a direction corresponding to the [111] direction of the diamond unit cell, i.e. along the NV spin quantization axis. The sensor is placed at a distance d below the flake and scanned in the x-y plane and the B-field projection onto the sensor z-axis is calculated to obtain a simulated image $B_{\text{sim}}(x, y, d)$. We then perform simulations of $B_{\text{sim}}(x, y, d)$ over the range of d_{NV} spanned by the NV depth probability distribution function $P(d_{\text{NV}})$ (Fig S2) and calculate an ensemble averaged image $B_{\text{simens}}(x, y) = \int B_{\text{sim}}(x, y, d_{\text{NV}})P(d_{\text{NV}})dd_{\text{NV}}$. Finally, the ensemble averaged image $B_{\text{simens}}(x, y)$ is convolved with a 2D Gaussian representing the optical diffraction limited width for a beam waist radius of $\sim 500\text{ nm}$ to generate the image shown in Fig 1d of the main text.

IV. TEMPERATURE RANGE OF SPIN ECHO NORMALIZATION

At temperatures near the CrSBr phase transition, we observed a decrease in the pulsed ODMR contrast in the interior region of the CrSBr flake relative to the contrast outside the flake (Figure S10a). This effect is consistent with the formation of sub-diffraction-limited static magnetic domains in the flake interior near the T_C as reported in few-layer CrSBr by Tschudin *et al.* with scanning NV magnetometry [31], which we would expect to broaden the inhomogeneous linewidth (Γ) of the NV ensemble probed by the diffraction-limited laser spot in our experiment. Changes in the ratio of the Rabi frequency Ω to the inhomogeneous linewidth Γ with temperature could affect the signal contrast in spin echo experiments [64], complicating the comparison of data across a broad temperature range.

In the following analysis we show that, based on the variation in pulsed ODMR contrast in the temperature range of $\sim 130 - 140$ K, we do not expect spin echo contrast to vary significantly enough to affect the analysis of the decoherence dynamics discussed in the main text. In particular, we show that the measured pulsed ODMR contrast (Figure S10a) can be used as a proxy to determine the ratio Ω/Γ at all temperatures. We then perform numerics to simulate the spin echo protocol at each value of Ω/Γ and demonstrate that the maximum effect on the normalized spin echo contrast is negligible.

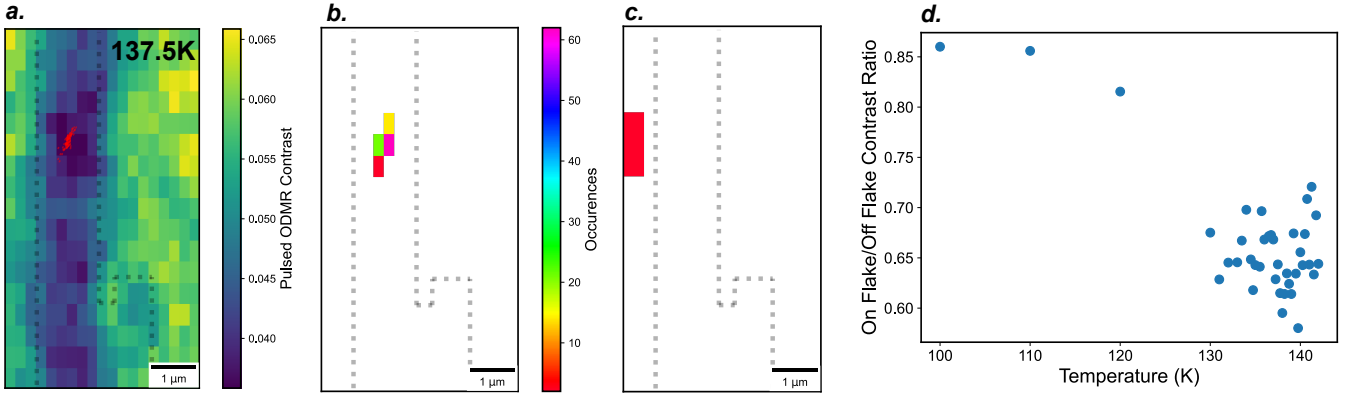


FIG. S10. (a.) Pulsed ODMR contrast image (see Section II D) with points sampled during spin echo measurements overlayed in red. (b.) Histogram of points sampled during spin echo measurements. (c.) Pixels selected to evaluate "off-flake" pulsed ODMR contrast. (d.) Ratio of pulsed ODMR contrast from "on-flake" vs. "off-flake" positions as a function of temperature.

We begin by comparing the pulsed ODMR contrast in the interior and exterior regions of the flake as a function of temperature. Since the Rabi frequency Ω is fixed across all measurements, this comparison will allow us to evaluate temperature-dependent changes in the inhomogeneous broadening Γ within the flake to the (temperature-independent) reference value outside the flake Γ_0 . We use our drift correction method (Section II E) to track the spread of spatial points sampled over the total course of spin echo measurements at 137.5 K, which is shown by the red dots overlayed on the pulsed ODMR contrast image in Figure S10a. From the spread of points we determine the probability that a pixel in the image was sampled during the spin echo measurement (Figure S10b) and calculate an average pulsed ODMR contrast for those points, obtained at Ω/Γ . We also calculate an average pulsed ODMR contrast for a region of pixels off of the flake obtained at Ω/Γ_0 (Figure 10c) and determine the ratio of on-flake/off-flake pulsed ODMR contrast. This process is repeated for the data taken at all temperatures and the ratio of on-flake/off-flake pulsed ODMR contrast as a function of temperature is shown in Figure S10d.

Next, we demonstrate that the ODMR contrast ratio plotted in Figure S10d is a valid proxy for the ratio Γ/Γ_0 . We begin by simulating the Rabi contrast for an inhomogeneously broadened NV ensemble. We model the two-level dynamics of the pseudo-spin-1/2 subspace of the NV ground state [65, 66] using QISKit DYNAMICS [67], where we define a rotating frame Hamiltonian in the S_z basis with eigenstates $|\alpha\rangle = \begin{pmatrix} 1 \\ 0 \end{pmatrix}$ and $|\beta\rangle = \begin{pmatrix} 0 \\ 1 \end{pmatrix}$:

$$H = h_z s_z + h_x s_x \quad (S1)$$

where s_z and s_x are the Pauli spin-1/2 operators, $h_x = 2\pi\Omega$ (where Ω is the Rabi frequency), and h_z is the off-resonance Zeeman energy. In each simulation the initial state is set to $|\psi_0\rangle = |\alpha\rangle$ and the state is evolved over time (in units of $t_{2\pi} = 1/\Omega$). To simulate Rabi oscillations for different ratios of Ω/Γ , we set the Rabi frequency $\Omega = 1$ for all simulations and randomly select values of h_x from a normal distribution of width $2\pi\Gamma$. For a given normal distribution, we simulate the dynamics for $> 10^3$ values of h_z , calculating the expectation value $\langle S_z \rangle = \frac{1}{2}(|c_\alpha|^2 - |c_\beta|^2)$

at each time point for each value of h_z . We then average the results over all values of h_z to compute the ensemble averaged expectation value $\langle S_z \rangle_{ens}$, and take $\frac{1}{2} + \langle S_z \rangle_{ens}$ as the simulated contrast [65]. Simulations are performed for a range of Γ from $0.1 - 10$. Figure S11a shows the simulated Rabi oscillations for two values of Ω/Γ , which are fit to a function of the form:

$$Ae^{-t/T_{\text{Rabi}}} \cos(2\pi\Omega t) + B \quad (\text{S2})$$

where T_{Rabi} is a time constant for the Rabi decay. Figure S11b shows T_{Rabi} (in units of $t_{2\pi}$) determined for a wide range of Ω/Γ . Figures S11c,d show the Rabi oscillations measured at on-flake and off-flake positions at 137.5K . By fitting the data in Figures S11c,d we extract a decay time T_{Rabi} in units of $t_{2\pi}$, from which we can determine values of Ω/Γ by interpolating Figure S11b. We determine a value of $\Omega/\Gamma = 3.1$ for the off-flake position and $\Omega/\Gamma = 1.03$ for the on-flake position at 137.5K . Next we determine the contrast for a π -pulse by evaluating $\frac{1}{2} + \langle S_z \rangle_{ens}$ at $t = 0.5$ from the Rabi oscillation simulations. Figure S11e shows the simulated π -pulse contrast as a function of Ω/Γ . Using the on-flake and off-flake Ω/Γ values at 137.5K determined above, we use Figure S11e to estimate the value for the ratio of on-flake/off-flake π -pulse ODMR contrast. We determine an estimated value of 0.58, which is in good agreement with the experimental value of 0.64 at 137.5K (Figure S10d). Assuming that the off-flake $\Omega/\Gamma_0 = 3.1$ is temperature independent, we then use the ratios of measured on-flake/off-flake pulsed ODMR contrast from Figure S10d to estimate the values of the on-flake Ω/Γ ratio at all temperatures (Figure S11f).

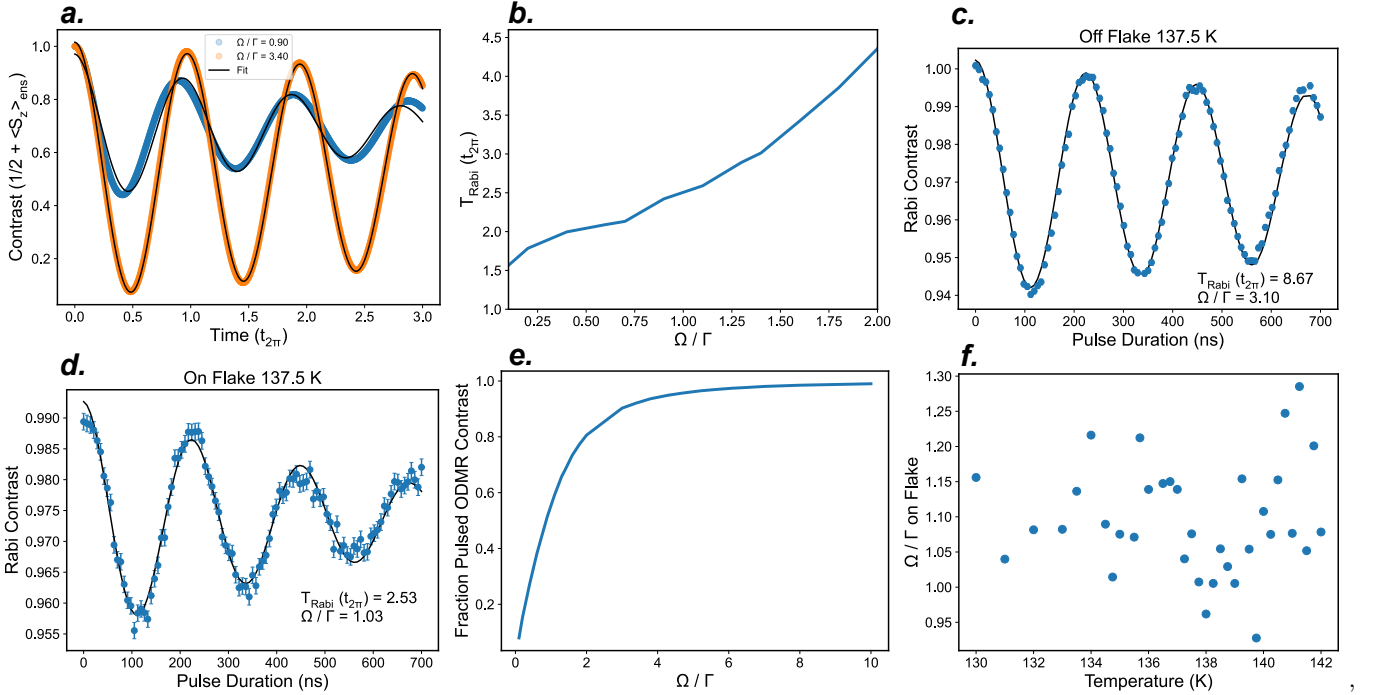


FIG. S11. (a.) Simulated Rabi contrast for two values of Ω/Γ with fits to Eq (2). (b.) Simulated T_{Rabi} as a function of Ω/Γ . (c.) & (d.) Rabi oscillations measured at positions on and off the CrSBr flake at 137.5 K , from which T_{Rabi} and Ω/Γ are determined. (e.) Simulated π -pulsed ODMR contrast as a function of Ω/Γ . (f.) Ω/Γ at the position on the CrSBr flake sampled in spin echo measurements as a function of temperature.

In order to understand the effect of the trend in Figure S10d on spin echo measurements, we determine an approximate relationship between the on-flake/off-flake pulsed ODMR contrast and initial spin contrast by performing a master equation simulation of spin echo as a function of Ω/Γ . We define a time-dependent Hamiltonian to simulate coherent driving in a spin echo $\frac{\pi}{2}(x) \rightarrow \pi(y) \rightarrow \frac{\pi}{2}(x, -x)$ pulse sequence with zero interpulse delay:

$$H = h_z s_z + H_1(t) \quad (\text{S3})$$

$$H_1(t) = 2\pi\Omega \begin{cases} s_x & 0 \leq t \leq \frac{1}{4} \\ s_y & \frac{1}{4} \leq t \leq \frac{3}{4} \\ s_{x,-x} & \frac{3}{4} \leq t \leq 1 \end{cases}$$

Here two simulations are performed: one with a final s_x rotation and one with a final s_{-x} rotation. Using a similar method to model inhomogeneous broadening as described above, we fix $\Omega = 1$ and perform simulations over randomly selected values of h_z taken from a normal distribution of width $2\pi\Gamma$, and evaluate the results for different values of Γ . In each simulation the initial spin echo contrast is defined as $\langle S_z \rangle_{echo} = \langle S_z \rangle_x - \langle S_z \rangle_{-x}$, evaluated at $t = 1$ (in units of $t_{2\pi}$). For each value of Γ we average the contrast for all values of h_z to determine the ensemble averaged spin echo contrast $\langle S_z \rangle_{ens_{echo}} = \langle S_z \rangle_{ens_x} - \langle S_z \rangle_{ens_{-x}}$. Figure S12a shows the simulated initial spin echo contrast as a function of Ω/Γ . Using the temperature-dependent values of the on-flake Ω/Γ determined above (Figure S11f), we interpolate Figure S12a to estimate the fraction of spin echo contrast lost at each temperature in our experiment (Figure S12b), which shows that there is not a strong trend of spin echo contrast loss with temperature in the range of $130 - 142K$. We quantify the spread of spin echo contrast loss in the range of $130 - 142K$ with a histogram (Figure S12c) which shows a variation of around 5% relative change the mean value of contrast loss (0.68).

To understand how this variation in spin echo contrast loss could impact the data, we compared two sets of temperature-normalized spin echo coherence decays $C_{T_{Norm}}(\tau)$: one with the raw data at all temperatures normalized relative to the raw data at $T_{Norm} = 131K$, and one with raw the data at each temperature scaled by a relative correction factor prior to normalization based on the estimated temperature dependent contrast loss from Figure S12b. Figures S12d,e show that there is little difference in the temperature normalized data with or without a correction for contrast loss. We also fit both the corrected and uncorrected data sets to stretched exponential functions and compare the temperature dependence of the extracted $\frac{1}{TT_2}$ rates and stretch parameters p . Figures S12f,g show that the trends in $\frac{1}{TT_2}$ and p observed at criticality are nearly identical with or without a contrast correction, indicating that our analysis of the spin echo dynamics at criticality is not likely to be impacted by changes in spin echo contrast.

Finally, we verify that the effect of the Ω/Γ ratio on spin manipulation does not affect the observed decoherence dynamics by simulating a $\frac{\pi}{2}(x) \rightarrow \tau \rightarrow \pi(y) \rightarrow \tau \rightarrow \frac{\pi}{2}(x, -x)$ spin echo sequence with pure dephasing and variable interpulse delay τ . Here we define a Hamiltonian:

$$H = h_z s_z + H_1(t) \quad (S4)$$

$$H_1(t) = 2\pi\Omega \begin{cases} s_x & 0 \leq t \leq \frac{1}{4} \\ s_y & \tau + \frac{1}{4} \leq t \leq \tau + \frac{3}{4} \\ s_{x,-x} & 2\tau + \frac{3}{4} \leq t \leq 2\tau + 1 \end{cases}$$

with t and τ in units of $t_{2\pi}$. To simulate pure dephasing we define a relaxation operator $\sqrt{\Gamma_2} s_z$ for the dissipative term of the Lindblad equation which causes the off-diagonal elements of the density matrix to decay at a rate $2\Gamma_2$. Simulations for a range of Ω/Γ are performed in the same way as above for the initial spin echo contrast, with $\Omega = 1$ and $\Gamma_2 = 0.3$ fixed for all simulations. Figure S12h shows the results of simulations for three different values of Ω/Γ . Figure S12i shows the simulations normalized to the value of $\langle S_z \rangle_{echo}$ at $\tau = 0$, which shows that the measured decoherence dynamics in the $\frac{\pi}{2}(x) \rightarrow \tau \rightarrow \pi(y) \rightarrow \tau \rightarrow \frac{\pi}{2}(x, -x)$ spin echo pulse sequence are not changed by the effect of Ω/Γ on spin manipulation.

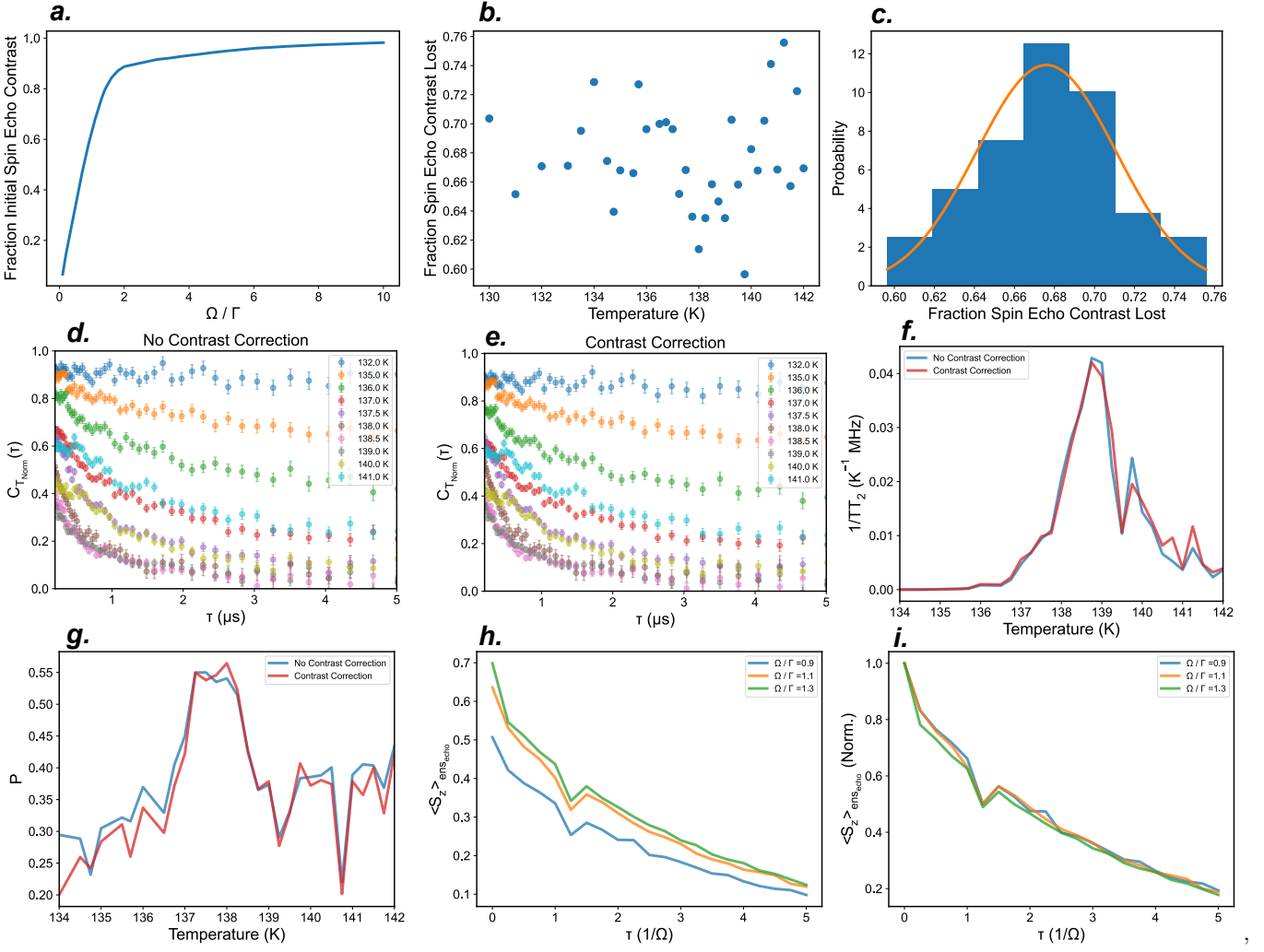


FIG. S12. (a.) Simulated initial spin echo contrast as a function of Ω/Γ . (b.) Spin echo contrast lost as a function of temperature determined from the values of Ω/Γ at the position on the CrSBr flake sampled in spin echo measurements. (c.) Histogram of the spin echo contrast loss from (b) and fit to a normal distribution. (d.), (e.), (f.), & (g.) Comparisons of $C_{T_{Norm}}(\tau)$ (for $T_{Norm} = 131K$) and $\frac{1}{T_2}$ and p stretched exponential fit parameters for raw spin echo data and for data corrected for a relative change in contrast based on (b). (h.) & (i.) Simulated spin echo coherence decays for different values of Ω/Γ .

V. CRITICAL DYNAMICS ANALYSIS

A. Simulation Methods and Definitions

We simulated the ensemble decoherence from the mean-field derived structure functions following the derivations from Machado *et al.* [15]. We start with the calculation of $\langle \phi^2 \rangle$ for a single NV center at a depth d from the 2D flake, given by:

$$\langle \phi^2 \rangle = \int_{\omega_L}^{\omega_U} W_\tau(\omega) \frac{d\omega}{2\pi} \int_0^{1/a} W_d(q) S(q, \omega) \frac{dq}{2\pi} \quad (\text{S5})$$

with:

$$W_\tau(\omega) = \left(\frac{2g_e\mu_B}{\hbar}\right)^2 \frac{\sin\left(\frac{\omega\tau}{4}\right)^4}{\omega^2} \quad (\text{S6})$$

where g_e is the electron g-factor and μ_B is the Bohr magneton, and:

$$W_d(q) = \frac{(\mu_0\mu_B g_e S)^2}{4a^4} q^3 e^{-2qd} \quad (\text{S7})$$

where μ_0 is the vacuum permittivity, $S = \frac{3}{2}$ is the electron spin for Cr^{3+} [25], and $a = 4.7485 \text{ \AA}$ is taken as the CrSBr lattice constant [26]. The limits on the first integral in (5) are set by the approximate width of the spin echo filter function $\omega_L = \frac{\pi-1}{\tau}$ and $\omega_U = \frac{\pi+1}{\tau}$ [15]. Restating from the main text we have:

$$S(q, \omega) = \frac{2k_B T \Gamma_0}{\Gamma_0^2 J^2 (\xi^{-2} + q^2)^2 + \omega^2} \quad (\text{S8})$$

where J is the exchange energy and Γ_0 is the kinetic coefficient defined as $\Gamma_0 = \frac{\omega_0}{J\xi_0^2}$ where ω_0 is a low temperature characteristic fluctuation frequency which can be compared with low temperature magnon frequencies reported in the literature [39] and ξ_0 is a low temperature fluctuation correlation length taken as $2a$ [15]. The temperature dependent correlation length ξ is defined as:

$$\xi = \xi_0 \left| \frac{T - T_C}{T_C} \right|^{-\nu} \quad (\text{S9})$$

where T_C is the critical temperature and ν is the critical exponent for the fluctuation correlation length. From the structure function (8) we also define the characteristic frequency $\omega_c(q)$ [15]:

$$\omega_c(q) = \Gamma_0 J (\xi^{-2} + q^{-2}) \quad (\text{S10})$$

where $\omega_c(q)$ is related to the fluctuation correlation time τ_c by $\omega_c(q) = \tau_c(q)^{-1}$ which is used to determine $\tau_c(q)^{-1}$ in Figures 4b,c of the main text. The coherence for a single NV is defined as:

$$C(\tau) = e^{-\frac{1}{2}\langle \phi^2 \rangle} \quad (\text{S11})$$

To model an ensemble averaged coherence, we calculate the expectation value for $C(\tau)$ over the probability distribution function for the NV depth ($P(d_{NV})$) determined from the C-TRIM simulation (Figure S2):

$$C^{ens} = \int e^{-\frac{1}{2}\langle \phi^2 \rangle_{d_{NV}}} P(d_{NV}) dd_{NV} \quad (\text{S12})$$

The depth dependence of $\langle \phi^2 \rangle$ comes in via (7) and is indicated explicitly by the notation $\langle \phi^2 \rangle_{d_{NV}}$. We perform simulations for 51 different NV depths d_{NV} spanning the range covered by $P(d_{NV})$ in Figure S2 and numerically calculate C^{ens} from (12). The ensemble averaged variance of the stochastic phase $\langle \phi^2 \rangle^{ens}$ is then defined as:

$$\langle \phi^2 \rangle^{ens} = -2\ln(C^{ens}) \quad (\text{S13})$$

We calculate the temperature normalized coherence $C_{T_{Norm}}^{ens}$ and variance of the stochastic phase $\langle \phi^2 \rangle_{T_{Norm}}^{ens}$ as:

$$C_{T_{Norm}}^{ens} = \frac{C_T^{ens}}{C_{T_{Ref}}^{ens}} \quad (\text{S14})$$

$$\langle \phi^2 \rangle_{T_{Norm}}^{ens} = -2 \ln(C_{T_{Norm}}^{ens}) \quad (S15)$$

which we use for the fits in Figure 4a of the main text.

The numerical integration of (5) is time consuming to the extent that it is unfeasible to use gradient optimization routines and a cost function to vary parameters J , ω_0 and ν over a range of d for determining best fit models of $\langle \phi^2 \rangle_{T_{Norm}}^{ens}$ to the data. Instead, we build a library of simulations for $\langle \phi^2 \rangle_{T_{Norm}}^{ens}$ over ranges of parameter values for J , ω_0 and ν . We then determine the best fit by selecting the parameter values that give the minimum of a global χ_{tot}^2 metric that evaluates the overall goodness-of-fit to the global set of temperature dependent data, which is defined as $\chi_{tot}^2 = \sqrt{(\chi_{T_1}^2)^2 + (\chi_{T_2}^2)^2 + \dots + (\chi_{T_N}^2)^2}$ where $\chi_{T_N}^2$ is the χ^2 value for the data at temperature T_N . As described in the main text, we fit the $\langle \phi^2 \rangle_{T_{Norm}}^{ens}$ data using a set of four temperatures 137.25 K, 137.5 K, 137.75 K, 138 K where we expect to see mean-field predicted critical slowing down based on the trend of the stretch power from stretched exponential fits to the decoherence (main text, Figure 3d inset).

B. Fit Comparisons

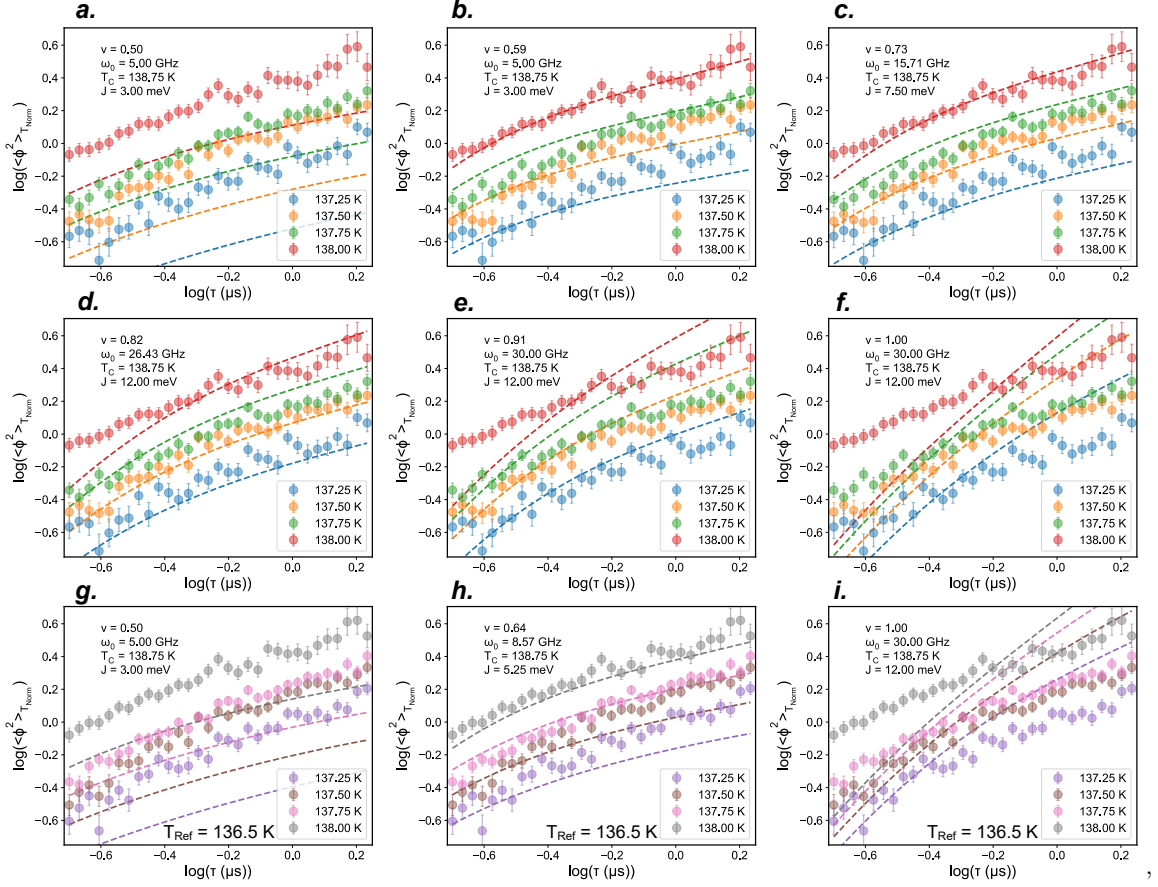


FIG. S13. To determine the sensitivity of the fits to the parameter ν , we fixed ν to values in the range of 0.5-1 (note $\nu_{Ising} = 1$) and allowed the parameters J and ω_0 to vary within reasonable ranges for the simulations of $\langle \phi^2 \rangle_{T_{Norm}}^{ens}$ using $T_C = 138.75$ K and $T_{Ref} = 136.75$ K. (a), (b), (d-f) Fits with the parameter ν fixed at 0.5, 0.59, 0.82, 0.91, and 1, respectively, whereas (c) shows the fits from Figure 4a in the main text with ν allowed to vary to a best fit value of $\nu = 0.73$. Only fits with fixed values of ν in the range of $\sim 0.6 - 0.8$ can reproduce the trend of the data. Note that the fits in (f) correspond to the Ising trends shown in Figure 4a of the main text. We also evaluate the sensitivity of the fits to ν using a different $T_{Ref} = 136.5$ K near criticality (g-i). (g) & (i) Fits with ν fixed at 0.5 and 1, respectively; (h) shows a fit with ν allowed to vary to a best fit value of $\nu = 0.64$.

C. Effects of the NV Ensemble Depth Distribution on Decoherence Dynamics

In this section, we perform a simple calculation demonstrating how the observed stretch-power is controlled by the NV depth distribution in an ensemble sample. In general, the precise functional form depends on many details of the coherence dynamics, but a simple estimation can illustrate how different NV density distributions lead to different stretch exponents. To this end, let us assume that at a depth z , the NV coherence dynamics is given by a stretched exponential form:

$$C(z, t) = e^{-\lambda_0 t^p / z^a}$$

where λ_0 captures the overall coupling strength, $1/z^a$ captures the depth dependence of the coupling between the NV and the sample. The overall coherence can be estimated as follows: the NV remains coherent until $\lambda_0 t^p / z^a \gtrsim 1$. This implies that, at time t , the coherence signal is approximated by the fraction of NVs that are located at a depth $z > z^* = (\lambda_0 t^p)^{1/a}$. The resulting functional form is:

$$C_{\text{tot}}(t) \approx \int_{z^*}^{\infty} dz \rho(z) \quad (\text{S16})$$

Assuming a generic functional form $\rho(z) \propto z^{k_1} e^{-(z/\xi)^{k_2}}$, we can analyze the time dependence of the signal:

$$C_{\text{tot}}(t) \propto \int_{(\lambda_0 t^p)^{1/a}}^{\infty} dz z^{k_1} e^{-(z/\xi)^{k_2}} = \xi^{k_1+1} \int_{(\lambda_0 t^p)^{1/a}/\xi}^{\infty} dy y^{k_1} e^{-y^{k_2}} = \xi^{k_1+1} \frac{\Gamma_{\frac{1+k_1}{k_2}}(y_0^{k_2})}{k_2} \Big|_{y_0=(\lambda_0 t^p)^{1/a}/\xi} \quad (\text{S17})$$

$$\xrightarrow[t \rightarrow \infty]{} C_0 \exp \left[- \underbrace{t^{pk_2/a}}_{\text{stretch power}} \lambda_0^{k_2/a} \xi^{-k_2} \right] t^{(-k_2+1+k_1)p/a} \quad (\text{S18})$$

where C_0 is a normalization factor that depends on λ_0 and ξ , and the polynomial terms in Eq. S18 would manifest is a log-correction to the observed stretch-power. While a simple estimation, this calculation immediately highlights, for an ensemble sample, that the observed stretch exponent depends not only on the stretch exponent for a single NV (which is p), but also on how the NV couples to the sample (captured here by a) as well as the tail distribution of the NV depth (encoded in k_2).